INTERNATIONAL JOURNAL FOR NUMERICAL METHODS IN FLUIDS, VOL. 17, 755–786 (1993)

BUOYANCY-DRIVEN INSTABILITY IN A VERTICAL CYLINDER: BINARY FLUIDS WITH SORET EFFECT. PART II: WEAKLY NON-LINEAR SOLUTIONS

G. R. HARDIN* AND R. L. SANI

Department of Chemical Engineering and Center for Low-Gravity Fluid Mechanics and Transport Phenomena,
University of Colorado, Boulder, CO 80309, U.S.A.

SUMMARY

The buoyancy-driven instability of a monocomponent or binary fluid that is completely contained in a vertical circular cylinder is investigated, including the influence of the Soret effect for the binary mixture. The Boussinesq approximation is used, and weakly-non-linear solutions are generated via Galerkin's technique using an expansion in the eigensolutions of the associated linear stability problem. Various types of fluid mixtures and cylindrical domains are considered. Flow structure and associated heat transfer are computed and experimental observations are cited when possible.

KEY WORDS Stability Soret Buoyancy Bifurcation Non-linear

INTRODUCTION

In Reference 1, hereafter referred to as Part I, the stability of a binary mixture in a vertical cylinder heated from beneath in the presence of a gravitational field was reviewed, formulated mathematically and its stationary stability extensively studied via a linear stability analysis. While such a study leads to useful predictions for the onset of convection, it cannot yield a quantitative characterization of the finite-amplitude flow and concomitant transport observed experimentally. A weakly non-linear analysis is presented to predict the behaviour of the system under slightly supercritical conditions. Of special interest is the spatial structure and stability of time-independent flows near onset.

MATHEMATICAL DESCRIPTION

The system to be studied consists of a layer of non-reactive fluid that completely fills a vertical, circular cylindrical container heated from beneath, as illustrated in Figure 1. Making use of the Boussinesq approximation and the scaling factors introduced in Part I leads to the following non-dimensional equations, detailed in Part I, for determining the dimensionless velocity ($\mathbf{u}$),

---

* Current Address: National Institute of Standards and Technology, Mail Code 83801, 325 Broadway, Boulder, CO 80303, U.S.A.

0271–2091/93/210755–32$21.00

Received 25 June 1991
Revised 4 May 1993

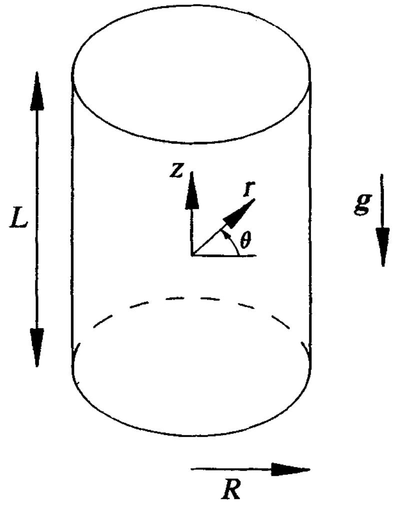

Figure 1. Cylindrical domain

pressure (p), temperature (T) and 'concentration' (η):

$$\frac{\partial \mathbf{u}}{\partial t}+\mathbf{u}\cdot\nabla\mathbf{u}=-\nabla p+(T-\psi\eta)\mathbf{e}_z+\nabla^2\mathbf{u}, \tag{1}$$

$$\tilde{Pr}\left(\frac{\partial T}{\partial t}+\mathbf{u}\cdot\nabla T\right)=\nabla^2 T+\zeta\nabla^2\eta+\tilde{Ra}(\mathbf{e}_z\cdot\mathbf{u}), \tag{2}$$

$$\tilde{Sc}\left(\frac{\partial \eta}{\partial t}+\mathbf{u}\cdot\nabla\eta\right)=\nabla^2 T+\nabla^2\eta, \tag{3}$$

$$\nabla\cdot\mathbf{u}=0, \tag{4}$$

where $\tilde{Ra}$, $\tilde{Pr}$ and $\tilde{Sc}$ are the Rayleigh, Prandtl and Schmidt numbers, respectively, modified for a binary mixture, ψ and ζ are parameters related to the Soret and Dufour effects, and $\mathbf{e}_z$ is the vertical unit vector. [Recall that ($\mathbf{u}$, T, η, p) represents a perturbation from a state of pure conduction and diffusion.] The appropriate boundary conditions are

$$\mathbf{u}=0, \quad \mathbf{n}\cdot\nabla T=0, \quad \mathbf{n}\cdot\nabla\eta=0, \quad \text{on } r=1, \quad -\tfrac{1}{2}<z<\tfrac{1}{2}, \tag{5}$$

$$\mathbf{u}=0, \quad T=0, \quad \mathbf{n}\cdot\nabla\eta=0, \quad \text{on } 0\leqslant r\leqslant 1, \quad z=\pm\tfrac{1}{2}. \tag{6}$$

Although in Part I the stability of cylinders with either a conducting or an insulating sidewall were both analysed, we now arbitrarily limit our focus to the insulating case. The extension to the conducting case is straightforward.

Note that η is a composite variable defined by

$$\eta=W_1+\left(\frac{\tilde{W}_1\tilde{W}_2 D'}{D}\right)T^{\mathrm{D}}$$

where W_1 is the (unscaled) local mass fraction of component 1 (which is usually taken to be the denser species), T^{D} is the dimensional temperature, $\tilde{W}_1$ and $\tilde{W}_2$ are the bulk mass fractions of the two components in the cylinder ($\tilde{W}_1+\tilde{W}_2=1$) and D' and D are the Soret and ordinary diffusion coefficients, respectively. η was introduced in Part I to decouple the boundary conditions: the zero-mass-flux boundary condition $D\mathbf{n}\cdot\nabla W_1+\tilde{W}_1\,\tilde{W}_2 D'\mathbf{n}\cdot\nabla T=0$ on all walls becomes $\mathbf{n}\cdot\nabla\eta=0$. Although the Dufour heat-flux term does not appear explicitly in the boundary conditions at the sidewall, an insulating sidewall is usually also assured because the combination of $\mathbf{n}\cdot\nabla T=0$ and $\mathbf{n}\cdot\nabla\eta=0$, in all but special cases, ensures that $\mathbf{n}\cdot\nabla W_1=0$, which eliminates the Dufour heat flux. However, the introduction of η is still useful because of the thermally conducting top and bottom.

While the cases studied here are limited to $\zeta=0$, i.e. neglecting the Dufour effect, the Dufour term is included since the solution technique is applicable for $\zeta\neq 0$. An approximate solution to this problem is found using a modified version of the weakly non-linear theory developed by Eckhaus.[2] Each solution $(\mathbf{u}, T, \eta)$ to the non-linear problem is approximated by a truncated series of eigenfunctions $(\mathbf{U}, \Theta, \Gamma)$ of the linear stability problem, augmented by a truncated series of eigenfunctions $(\mathbf{0}, \bar{\Theta}, \bar{\Gamma})$ of the linearized horizontally averaged problem as follows:

$$(\mathbf{u}, T, \eta)=\sum_{l=1}^{2}\sum_{n=0}^{N}F_{nl}(\mathbf{U}, \Theta, \Gamma)_{nl}+\sum_{t=1}^{2}\sum_{l=1}^{2}\sum_{j=0}^{J}H_{jlt}(\mathbf{0}, \bar{\Theta}, \bar{\Gamma})_{jlt}. \tag{7}$$

(See Reference 3 for details on the horizontally averaged problem, its adjoint problem and their solutions.) Each $(\mathbf{U}, \Theta, \Gamma)_{nl}$ represents a modal solution to the linear stability problem as generated in Part I with boundary conditions (5) and (6) and $\zeta=0$. [The pressure, p, does not explicitly appear here because the velocity-field representation is solenoidal. If desired, p may be computed once the $(\mathbf{u}, T, \eta)$ vector is known.] The value of n determines the azimuthal dependence of the modal solution, while the value of l determines its vertical symmetry (see Part I). Each $(\mathbf{0}, \bar{\Theta}, \bar{\Gamma})_{jlt}$ represents an eigenvector of the linearized, horizontally averaged transport equations for $\zeta=0$; these terms are necessary in order to obtain a physically reasonable non-linear approximation. The weakly-non-linear solutions must track the deformations of the horizontally averaged T and η fields corresponding to convective transport. All $(\mathbf{U}, \Theta, \Gamma)_{nl}$ yield zero horizontal averages for T and η owing to the $\cos(n\theta)$ azimuthal dependence of Θ and Γ, or, for $n=0$, to the design of the trial functions which automatically satisfy the derivative boundary conditions at the sidewall. (If the sidewalls were conducting, the $n=0$ mode would provide the sole exception, which would still be insufficient to track the deformations.)

For each approximate non-linear solution there exists a corresponding set of coefficients (F_{nl}, H_{jlt}). These coefficients are found by weighting the error (residual) of the approximate solutions by the eigenvectors of the associated adjoint problem to the linear stability problem since the latter is non-selfadjoint. In practice, only a small number of terms that are expected to have the largest amplitude coefficients are retained in the series (7); the criterion for selection of these terms was discussed by Rosenblat.[4] This constraint is based on practicality, but it limits the range in $\tilde{Ra}$ over which the solutions are quantitatively reliable to values near $\tilde{Ra}^{c}$.

The problem of interest is defined in equations (1)–(6). However, expansion (7) is comprised of separate expansions for $(\mathbf{u}, \hat{T}, \hat{\eta})$ and $(\mathbf{0}, \bar{T}, \bar{\eta})$, where $\hat{T}$ and $\hat{\eta}$ have zero horizontal averages, while $\bar{T}$ and $\bar{\eta}$ are functions of only the vertical co-ordinate (z) and time (t), such that $T=\hat{T}+\bar{T}$ and $\eta=\hat{\eta}+\bar{\eta}$. Consequently, problems (1)–(6) are recast explicitly in terms of $\hat{T}$, $\bar{T}$, $\hat{\eta}$ and $\bar{\eta}$, rather than T and η. Specifically, solutions $(\mathbf{u}, \hat{T}, \bar{T}, \hat{\eta}, \bar{\eta})$ are sought to the equations

$$\frac{\partial\mathbf{u}}{\partial t}+\mathbf{u}\cdot\nabla\mathbf{u}=-\nabla p+[\hat{T}+\bar{T}-\psi(\hat{\eta}+\bar{\eta})]\,\mathbf{e}_z+\nabla^2\mathbf{u}, \tag{8}$$

$$\tilde{Pr}\left[\frac{\partial\hat{T}}{\partial t}+\frac{\partial\bar{T}}{\partial t}+\mathbf{u}\cdot\nabla\hat{T}+(\mathbf{u}\cdot\mathbf{e}_z)\frac{\partial\bar{T}}{\partial z}\right]=\nabla^2\hat{T}+\frac{\partial^2\bar{T}}{\partial z^2}+\zeta\left[\nabla^2\hat{\eta}+\frac{\partial^2\bar{\eta}}{\partial z^2}\right]+\tilde{Ra}(\mathbf{u}\cdot\mathbf{e}_z), \tag{9}$$

$$\tilde{S}c\left[\frac{\partial\hat{\eta}}{\partial t}+\frac{\partial\bar{\eta}}{\partial t}+\mathbf{u}\cdot\nabla\hat{\eta}+(\mathbf{u}\cdot\mathbf{e}_z)\frac{\partial\bar{\eta}}{\partial z}\right]=\nabla^2\hat{T}+\frac{\partial^2\bar{T}}{\partial z^2}+\nabla^2\hat{\eta}+\frac{\partial^2\bar{\eta}}{\partial z^2}, \tag{10}$$

$$0=\nabla\cdot\mathbf{u}, \tag{11}$$

$$\tilde{P}r\left(\frac{\partial\bar{T}}{\partial t}+\overline{\mathbf{u}\cdot\nabla\hat{T}}\right)=\frac{\partial^2\bar{T}}{\partial z^2}+\zeta\frac{\partial^2\bar{\eta}}{\partial z^2}, \tag{12}$$

$$\tilde{S}c\left(\frac{\partial\bar{\eta}}{\partial t}+\overline{\mathbf{u}\cdot\nabla\hat{\eta}}\right)=\frac{\partial^2\bar{T}}{\partial z^2}+\frac{\partial^2\bar{\eta}}{\partial z^2}. \tag{13}$$

Here the overline denotes a horizontally averaged quantity. The corresponding boundary conditions are

$$\mathbf{u}=0,\qquad \mathbf{n}\cdot\nabla\hat{T}=0,\qquad \mathbf{n}\cdot\nabla\hat{\eta}=0\quad\text{on } r=1,\ -\tfrac{1}{2}\leqslant z\leqslant\tfrac{1}{2}, \tag{14}$$

$$\mathbf{u}=0,\qquad \hat{T}=0,\qquad \mathbf{n}\cdot\nabla\hat{\eta}=0\quad\text{on } 0\leqslant r\leqslant 1,\ z=\pm\tfrac{1}{2}, \tag{15}$$

$$\bar{T}=0,\quad \frac{\partial\bar{\eta}}{\partial z}=0\quad z=\pm\tfrac{1}{2}. \tag{16}$$

Each of the field variables $\mathbf{u}$, $\hat{T}$ and $\hat{\eta}$ corresponds to a field variable from the linear stability problem $\mathbf{U}$, Θ or Γ, respectively, which in turn each correspond to a field variable from the linear adjoint stability problem $\mathbf{U}^*$, Θ^* or Γ^*, respectively. (See Reference 3 for details on the linear adjoint system and its solutions. This problem was solved in the same fashion as the original linear stability problem.) In analogy with the Galerkin technique applied in Part I to the linear stability problem, an L_2 inner product (denoted by $\langle,\rangle$) is used to define the projection, and the same notation is used. However, in contrast to Part I, the adjoint eigenvectors $\mathbf{U}^*, \Theta^*, \Gamma^*, \bar{\Theta}^*$ and $\bar{\Gamma}^*$ are utilized in the projection of the residual functions, i.e. a Petrov–Galerkin method employing the adjoint eigenvectors is employed. The latter leads to some simplifications in the formulation due to orthogonality. Applying this procedure to equations (8)–(11) yields an equation for each index pair nl corresponding to a particular modal solution of the linear stability problem retained in expansion (7):

$$\begin{aligned}(\tilde{R}a-\tilde{R}a_{nl})\langle\Theta^*_{nl},(\mathbf{u}\cdot\mathbf{e}_z)\rangle={}&\left\langle\mathbf{U}^*_{nl},\left(\frac{\partial\mathbf{u}}{\partial t}+\mathbf{u}\cdot\nabla\mathbf{u}\right)\right\rangle\\&+\tilde{P}r\left\langle\Theta^*_{nl},\left(\frac{\partial\hat{T}}{\partial t}+\frac{\partial\bar{T}}{\partial t}+\mathbf{u}\cdot\nabla\hat{T}+(\mathbf{u}\cdot\mathbf{e}_z)\frac{\partial\bar{T}}{\partial z}\right)\right\rangle\\&+\tilde{S}c\left\langle\Gamma^*_{nl},\left(\frac{\partial\hat{\eta}}{\partial t}+\frac{\partial\bar{\eta}}{\partial t}+\mathbf{u}\cdot\nabla\hat{\eta}+(\mathbf{u}\cdot\mathbf{e}_z)\frac{\partial\bar{\eta}}{\partial z}\right)\right\rangle,\end{aligned} \tag{17}$$

where $\mathbf{U}^*_{nl}$, Θ^*_{nl} and Γ^*_{nl} represent the adjoint field variables corresponding to those of the modal solution $(\mathbf{U},\Theta,\Gamma)_{nl}$. This equation gives the first type of constraint needed to determine the coefficients in expansion (7). Note that the pressure term has been eliminated and each velocity basis function is solenoidal, so that no specific representation of the pressure field is required.

Following an analogous procedure, the second type of constraint equation resulting from equations (12) and (13) is:

$$-\pi\xi_{jlt}\int_z(\bar{T}\bar{\Theta}^*_{jlt}+\bar{\eta}\bar{\Gamma}^*_{jlt})\,\mathrm{d}z=\tilde{P}r\left\langle\bar{\Theta}^*_{jlt},\left(\frac{\partial\bar{T}}{\partial t}+\overline{\mathbf{u}\cdot\nabla\hat{T}}\right)\right\rangle+\tilde{S}c\left\langle\bar{\Gamma}^*_{jlt},\left(\frac{\partial\bar{\eta}}{\partial t}+\overline{\mathbf{u}\cdot\nabla\hat{\eta}}\right)\right\rangle, \tag{18}$$

where ξ_{jlt} is an eigenvalue of the linearized horizontally averaged problem, and $\bar{\Theta}^*_{jlt}$ and $\bar{\Gamma}^*_{jlt}$ represent the adjoint field variables corresponding to the eigenvector $(0, \bar{\Theta}, \bar{\Gamma})_{jlt}$. One such equation is required for each index triplet jlt corresponding to an eigensolution of the linearized horizontally averaged problem retained in expansion (7).

Substituting representation (7) for $\mathbf{u}$, $\hat{T}$, $\hat{\eta}$, $\bar{T}$ and $\bar{\eta}$ into equations (17) and (18) gives the equations that must be solved for the coefficients (F_{nl}, H_{jlt}). Substituting the representations from expansion (7) into equation (17) yields

$$
\begin{aligned}
&\sum_{r,s}\sum_{j,k}[\langle \mathbf{U}^*_{rsmp}, \mathbf{U}_{jkmp}\rangle + \tilde{P}r\langle \Theta^*_{rsmp}, \Theta_{jkmp}\rangle + \tilde{S}c\langle \Gamma^*_{rsmp}, \Gamma_{jkmp}\rangle]\frac{\mathrm{d}F_{mp}}{\mathrm{d}t}\\
&\qquad +\sum_{r,s}\sum_{j,l,t}[\tilde{P}r\langle \Theta^*_{rsmp}, \bar{\Theta}_{jlt}\rangle + \tilde{S}c\langle \Gamma^*_{rsmp}, \bar{\Gamma}_{jlt}\rangle]\frac{\mathrm{d}H_{jlt}}{\mathrm{d}t}\\
&\qquad = F_{mp}(\tilde{R}a - \tilde{R}a_{mp})\sum_{r,s}\sum_{j,k}\langle \Theta^*_{rsmp}, (\mathbf{U}_{jkmp}\cdot\mathbf{e}_z)\rangle\\
&\qquad\quad -\sum_{r,s}\sum_{a,b,c,d}\sum_{j,k,n,l}\{\langle \mathbf{U}^*_{rsmp}, [(\mathbf{U}_{abcd}\cdot\nabla)\mathbf{U}_{jknl}]\rangle\\
&\qquad\quad + \tilde{P}r\langle \Theta^*_{rsmp}, [(\mathbf{U}_{abcd}\cdot\nabla)\Theta_{jknl}]\rangle + \tilde{S}c\langle \Gamma^*_{rsmp}, [(\mathbf{U}_{abcd}\cdot\nabla)\Gamma_{jknl}]\rangle\} F_{cd}F_{nl}\\
&\qquad\quad -\sum_{r,s}\sum_{a,b,c,d}\sum_{j,l,t}\left\{\tilde{P}r\left\langle \Theta^*_{rsmp}, \left[(\mathbf{U}_{abcd}\cdot\mathbf{e}_z)\frac{\mathrm{d}\bar{\Theta}_{jlt}}{\mathrm{d}z}\right]\right\rangle\right.\\
&\qquad\quad \left. + \tilde{S}c\left\langle \Gamma^*_{rsmp}, \left[(\mathbf{U}_{abcd}\cdot\mathbf{e}_z)\frac{\mathrm{d}\bar{\Gamma}_{jlt}}{\mathrm{d}z}\right]\right\rangle\right\} F_{cd}H_{jlt}.
\end{aligned}
\tag{19}
$$

Substituting representation (7) into equation (18) gives

$$
\begin{aligned}
&\sum_{j,l,t}[\tilde{P}r\langle \bar{\Theta}^*_{kps}, \bar{\Theta}_{jlt}\rangle + \tilde{S}c\langle \bar{\Gamma}^*_{kps}, \bar{\Gamma}_{jlt}\rangle]\frac{\mathrm{d}H_{jlt}}{\mathrm{d}t}\\
&\qquad = -\pi\xi_{kps}\sum_{j,l,t}\left\{\int_z (\bar{\Theta}^*_{kps}\bar{\Theta}_{jlt} + \bar{\Gamma}^*_{kps}\bar{\Gamma}_{jlt})\,\mathrm{d}z\right\} H_{jlt} - \sum_{a,b,c,d}\sum_{j,k,n,l}\{\tilde{P}r\langle \bar{\Theta}^*_{kps}, [(\mathbf{U}_{abcd}\cdot\nabla)\Theta_{jknl}]\rangle\\
&\qquad\quad - \tilde{S}c\langle \bar{\Gamma}^*_{kps}, [(\mathbf{U}_{abcd}\cdot\nabla)\Gamma_{jknl}]\rangle\Big\} F_{cd}F_{nl}.
\end{aligned}
\tag{20}
$$

Note that the volume integration inherent in the L_2 inner product over the cylindrical domain automatically takes care of the necessary horizontal averaging of the non-linear terms in this equation, and many of the linear terms will be zero as a result of orthogonality. In these equations,

$$
\left.\begin{aligned}
\mathbf{U}^*_{jknl} &= A^*_{jknl}\mathbf{V}_{jknl} + D^*_{jknl}\mathbf{W}_{jknl}\\
\mathbf{U}_{jknl} &= A_{jknl}\mathbf{V}_{jknl} + D_{jknl}\mathbf{W}_{jknl}
\end{aligned}\right\} \text{(3D)},
\tag{21}
$$

or

$$
\left.\begin{aligned}
\mathbf{U}^*_{jknl} &= A^*_{jknl}\mathbf{O}_{jknl}\\
\mathbf{U}_{jknl} &= A_{jknl}\mathbf{O}_{jknl}
\end{aligned}\right\} \text{(2D axisymmetric, } n=0\text{)},
\tag{22}
$$

and

$$
\Theta^*_{jknl} = B^*_{jknl}\Phi_{jknl}, \qquad \Theta_{jknl} = B_{jknl}\Phi_{jknl},
\tag{23}
$$

$$
\Gamma^*_{jknl} = C^*_{jknl}\Lambda_{jknl}, \qquad \Gamma_{jknl} = C_{jknl}\Lambda_{jknl},
\tag{24}
$$

where $\mathbf{V}_{jknl}, \mathbf{W}_{jknl}, \mathbf{O}_{jknl}, \mathbf{\Phi}_{jknl}$ and Λ_{jknl} are basis functions defined in Part I. In addition, $(\mathbf{0}, \bar{\Theta}_{jlt}, \bar{\Gamma}_{jlt})$ and $(\mathbf{0}, \bar{\Theta}^*_{jlt}, \bar{\Gamma}^*_{jlt})$ are the eigenvectors and adjoint eigenvectors, respectively, of the spatially averaged operators. The subscript l, which was not used in Part I, denotes the even ($l=1$) or odd ($l=2$) solutions since both are needed in the weakly non-linear expansion. (More details on the index notation are given in Part I and Reference 3.)

The system of algebraic equations resulting from equations (19) and (20) are used to study the steady-state solution branches as $\tilde{Ra}$ is varied for specific fluid mixtures (represented by specific values of ψ, $\tilde{Pr}$ and $\tilde{Sc}$) at selected (radius-to-height) aspect ratios (γ). Thus, a system of coupled non-linear algebraic equations for the set of coefficients (F_{nl}, H_{jlt}) must be solved for each steady state sought. The integrals in equations (19) and (20) were evaluated using Gaussian quadrature with error control. The resulting system of algebraic equations are solved using Newton's method with an exact Jacobian and branches tracked via first-order continuation.

Since expansion (7) is composed of solutions to linear problems that are independent of $\tilde{Pr}$ and $\tilde{Sc}$,[1] the set of integrals in equations (19) and (20) need not be re-evaluated as these parameters are varied for fixed values of γ and ψ. This greatly improves the efficiency of this technique in studying the effects of these parameters. Moreover, $\tilde{Ra}$ can be varied in the same manner, which is extremely useful in terms of making this an efficient technique for tracking solution branches as $\tilde{Ra}$ is varied via, for example, continuation schemes.

The criterion proposed by Rosenblat[4] for truncation of an eigenfunction expansion of the field variables in a non-linear stability problem is based on the linear stability results for the modal excitation energies (as expressed here in terms of the modal Rayleigh numbers $\tilde{Ra}_{nl}$) and the possible quadratic self-interactions of the critical mode. From the linear stability results for the problem,[1] it is seen that in the aspect ratio range $0 \leqslant \gamma \leqslant 4$ usually either the $n=0$ ($l=1$) or $n=1$ ($l=1$) mode is the critical mode for the onset of convection, with the $n=2$ ($l=1$) mode playing a lesser role. Also, these modes generally have the three lowest energies over this range of aspect ratios. Consequently, in order to study the evolution of the primary solution branches (i.e. branches bifurcating from the conduction state) as $\tilde{Ra}$ is varied near the critical value for each set of parameters ($\tilde{Pr}$, $\tilde{Sc}$, ψ, γ), it is convenient to generate the integrals needed in equations (19) and (20) for the same set of eigenfunctions for each set of parameters (ψ, γ) studied. So, for each set of values of (ψ, γ) studied, the solution to the non-linear problem is expanded in terms of equation (7) using the same set of eigenfunctions from the linear stability problem, since this set of functions, along with a suitable set of mean-field eigenfunctions, is capable of representing all of the desired primary solution branches sufficiently close to the onset of convection. For the cases considered here, all of the primary branches can be represented in terms of modes selected from the same set of six modes, namely, the three modes specified above plus their $l=2$ counterparts (along with an appropriate set of mean-field eigenfunctions). Consequently, it is always convenient to compute the terms in the constraint equations (19) and (20) as if the non-linear solution were to be expanded in terms of six modes, and then to seek solutions of the resulting algebraic system for which various subsets of the coefficients (F_{nl}, H_{jlt}) are taken to be zero, corresponding to different branches. In addition, it is expected that for solutions near the critical Rayleigh number on any branch, the amplitude coefficients H_{jlt} in the representation of the mean fields $\bar{T}$ and $\bar{\eta}$ will decrease in magnitude for increasing j (i.e. higher harmonics). This expectation is based on the physical reasoning that thin conduction boundary layers will not form at the top and bottom of the container until the flow is much more vigorous than it is anticipated to be in the Rayleigh number range of interest. These considerations lead to the following form of expansion (7):

$$(\mathbf{u}, T, \eta) \cong \sum_{l=1}^{2} \left[\sum_{n=0}^{2} F_{nl}(\mathbf{U}, \Theta, \Gamma)_{nl} + \sum_{t=1}^{2} \sum_{j=0}^{J} H_{jlt}(\mathbf{0}, \bar{\Theta}, \bar{\Gamma})_{jlt} \right], \tag{25}$$

where J is varied depending on the number of terms required to achieve the desired convergence. In general, J must be increased as $\tilde{Ra}$ is increased. Using expansion (25) provides a significant advantage over strictly following the truncation criterion espoused[4] and used[5,6] by Rosenblat and co-workers. Rather than having the form of each solution completely determined by an *a priori* selection of a minimal set of modes in expansion (7), the use of a slightly larger, though nonetheless judiciously chosen, set of modes allows for a greater possible number of solutions. While the forms of primary branches can be aptly determined by Rosenblat's criterion, a good set of modes for the representation of secondary branches (i.e. those that bifurcate from primary branches) would be much more difficult to select. Consequently, the approach used here appears more likely to suggest potential secondary bifurcations. Furthermore, it is hoped that by including more modes it might be possible to extend the analysis to higher Rayleigh numbers than would otherwise be possible. Nonetheless, the choice of the six modes used in expansion (7) is based on Rosenblat's criterion.

In the presentation of the results, the steady-state solution branches are represented by graphs of the horizontally averaged Nusselt number (Nu) as a function of $\tilde{Ra}$. For the case of an insulating sidewall, the horizontally averaged heat transfer is independent of z at steady state. For clarity, the dimensionless temperature field is rescaled, with the linear field added back in, so that the Nusselt number has a value of unity for a state of pure conduction. The rescaling is as follows:

$$T^{\mathrm{R}} \equiv \frac{\tilde{Pr}}{\tilde{Ra}} T - z, \tag{26}$$

which can be rewritten in terms of *dimensional* temperatures, denoted here by a superscript D for clarity as

$$T^{\mathrm{R}} = \frac{(T^{\mathrm{D}} - \bar{T}^{\mathrm{D}})}{(T^{\mathrm{D}}_{\mathrm{B}} - T^{\mathrm{D}}_{\mathrm{T}})}, \tag{27}$$

where $\bar{T}^{\mathrm{D}} \equiv \frac{1}{2}(T^{\mathrm{D}}_{\mathrm{B}} + T^{\mathrm{D}}_{\mathrm{T}})$, with $T^{\mathrm{D}}_{\mathrm{T}}$ and $T^{\mathrm{D}}_{\mathrm{B}}$ being the temperatures at the top and bottom of the cylinder, respectively. Consequently, the Nusselt number can be interpreted as the degree of convective enhancement to the heat transfer. The horizontally averaged Nusselt number then has the following simple form in terms of the rescaled dimensionless temperature:

$$Nu = 1 + \left| \frac{\tilde{Pr}}{\tilde{Ra}} \frac{\partial \bar{T}}{\partial z} \right|, \tag{28}$$

where $\bar{T}$ still represents the deviation from the linear, conduction profile. Thus defined, the Nusselt number will always be positive ($Nu \geqslant 1$), regardless of whether heating is from the top or bottom, and the sign of the Nusselt number will not be used to specify the direction of heat transfer. There are primarily two reasons to use graphs of Nusselt number as a function of Rayleigh number for representation of the solution branches: first, this is the most common means of presenting results of experimental studies of incipient convection; second, it is a universal approach in that it can be used as a means of characterizing any thermoconvective flow state, regardless of the spatial variation of the flow field.

An extremely important characteristic of the steady-state convective solutions is their stability. This must be established in order to predict whether or not a given flow state will be observable in a real physical system. Fortunately, this is easily accomplished here by analysing the system of first order, non-linear differential equations represented by equations (19) and (20). For convenience, this system of equations is represented as follows:

$$\mathbf{M} \frac{\partial \mathbf{A}}{\partial t} = \mathbf{F}(\mathbf{A}), \tag{29}$$

where the matrix **M** results from the integrals multiplying the time-derivative terms, and **A** is a vector whose elements are the set of amplitude coefficients (F_{nl}, H_{jlt}). The algebraic problem for the steady-state solutions of equations (19) and (20) is then given by

$$\mathbf{F}(\mathbf{A}^s)=0, \tag{30}$$

where the vector $\mathbf{A}^s$ represents a particular set of values of the coefficients **A** corresponding to a particular steady state. The stability of a steady-state solution $\mathbf{A}^s$ is then found using linear stability theory, i.e. the solution is first written in the form

$$\mathbf{A}=\mathbf{A}^s+\mathbf{A}^d e^{\chi t}, \tag{31}$$

where $\mathbf{A}^d e^{\chi t}$ represents a disturbance to the steady state $\mathbf{A}^s$, and then linearized about the steady-state solution $\mathbf{A}^s$ to yield

$$\chi \mathbf{M}\mathbf{A}^d=\mathbf{J}\mathbf{A}^d, \tag{32}$$

where $\mathbf{J}\equiv(\partial \mathbf{F}/\partial \mathbf{A})_{\mathbf{A}^s}$ is the Jacobian associated with the solution of equation (30) via Newton's method. This problem is a generalized eigenvalue problem for χ. If any of the eigenvalues has a positive real part, the disturbance with the spatial form determined from the corresponding eigenvector $\mathbf{A}^d$ will grow exponentially in time, so the solution $\mathbf{A}^s$ is unstable. In this analysis the non-linear solutions are approximated by expansion (25), which is a truncation of expansion (7). Consequently, the stability of each steady-state solution $\mathbf{A}^s$ is only assessed with respect to a limited class of disturbances. Although stability is presumed if all of the eigenvalues of equation (32) are negative, it cannot be guaranteed.

DISCUSSION

The parameter space associated with the mathematical characterization of the problem is $(\gamma, \tilde{Ra}, \tilde{Pr}, \tilde{Sc}, \psi, \zeta)$. Clearly, it would be very difficult and time consuming to conduct a thorough investigation of the roles of each of these parameters over their entire range. Consequently, certain limitations are imposed to reduce the scope of this study. As previously discussed, the parameter ζ is neglected entirely, with the justification that it is expected to play a minor role. The Rayleigh number range of interest is that near the onset of convection. Monocomponent fluids are an important subclass of binary systems in several respects: they are a limiting case as $|\psi|\rightarrow 0$, and separate the physically disparate cases of fluid systems for which $\psi<0$ or $\psi>0$. Since monocomponent systems have not been thoroughly characterized previously, it is felt that an appropriate starting point for this analysis is to undertake this task. Consequently, monocomponent systems are used as the primary vehicle for studying the effect of varying the cylinder aspect ratio, γ. At the same time, to gain some insight into the effect of varying the Prandtl number, monocomponent systems corresponding to two Prandtl numbers are considered: $Pr=6{\cdot}7$, corresponding to water, which is somewhat intermediary between the 'typical' values for gases and liquids (approximately 1 and 100, respectively), and $Pr=0{\cdot}02$, which is a characteristic value for liquid metals. The numerical solutions for these Prandtl numbers are compared with the experimental results of Müller *et al.*,[7] who studied buoyancy-driven convection of water, and also of liquid gallium. In studying the effect of varying ψ, selected binary mixtures will be studied for which the Soret coefficient has been measured, and for which it is felt that the experimental results are reasonably reliable. The latter is by no means a trivial constraint. Finally, as a result of focusing on selected, real physical systems, an independent study of the effect of varying the Schmidt number is not undertaken; the Schmidt numbers that are studied are simply those corresponding to the binary systems for which Soret coefficients are available.

Monocomponent fluids

It is well documented, both theoretically (see e.g. References 1 and 8–10) and experimentally (see e.g. References 7 and 11), that the onset of convection in cylinders with small aspect ratios occurs in the form of a single antisymmetric roll cell. Such a flow is illustrated in Figure 2 for $Pr=6{\cdot}7$, $\gamma=1/7$ and $Ra=180\,300$, just after the onset of convection [Henceforth, only Rayleigh numbers based on the height of the cylinder (L) will be used (i.e. Ra or $\tilde{R}a$) in order to facilitate comparisons of results at different aspect ratios.] Computationally, the onset occurs at 180 290. There is no qualitative difference between this flow and the flow structure at the same Rayleigh number for $Pr=0{\cdot}02$, but the amplitude of the non-dimensional velocity field is greater for the low Prandtl number case, as expected. (Recall that the velocity scale is ν/L. See Reference 3 for details.)

For the case shown in Figure 2, the maximum velocity is located approximately in the vertical and horizontal midplane (i.e. at $z=0$ and $\theta=0$, or the antisymmetric equivalent) at a dimensionless radius (r/R, where R is the cylinder radius) of about 1/2. If we boldly (and without justification) increase the Rayleigh number to 300 000, the flow structure (Figure 3) is similar to the experimental observations of Müller *et al.*[7] at this Rayleigh number. The plane corresponding to $\theta=90°$ shows the initial stages of the generation of secondary recirculations; such two-dimensional (2D) projections must be interpreted with care since the main flow is perpendicular to this plane, with the speed of the projected velocities being an order of magnitude greater in the $\theta=0$ plane than in the $\theta=90°$ plane. This recirculation pattern is a direct consequence of the flow tilting in the cylinder so that it is not completely horizontal at $\theta=90°$, as it would be in the limit as $Ra\rightarrow Ra^c$. At $\theta=90°$, the flow is slightly upward at $r=0$ for $z>0$, but the main component of the velocity is horizontal.

The reason for this tilting is that as the faster moving fluid at $r\approx 1/2$, $\theta\approx 0$ approaches either the top or the bottom of the cylinder, the stagnation pressure forces it to turn more toward the far 'corner' until it is forced to turn downward. While most of the fluid that flows toward the middle of the top is carried forward, some of it is turned sideways, resulting in the secondary flow. As the

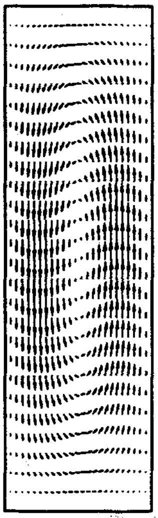

Figure 2. Cross section of flow near onset for $\gamma=1/7$ and $Pr=6{\cdot}7$ ($|\mathbf{u}|_{\max}=0{\cdot}056$)

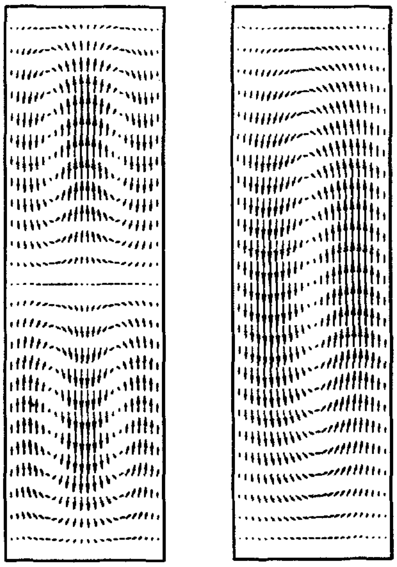

$\theta = 90°$ $\theta = 0$

Figure 3. Flow structure at $Ra=300\,000$ for $\gamma=1/7$ with $Pr=6{\cdot}7$ ($\theta=0°$, $|\mathbf{u}|_{\max}=6{\cdot}41$; $\theta=90°$, $|\mathbf{u}|_{\max}=0{\cdot}332$)

average speed of the fluid increases with increasing Rayleigh number, more of the fluid is diverted into the secondary recirculations. The maximum velocity is moved toward the sidewall relative to the lower Rayleigh number case because the increased flow speeds result in greater shear near $r=0$.

The bifurcation diagram for $Pr=6{\cdot}7$ is given in Figure 4. This figure shows that the one-cell solution that bifurcates from $Ra^c = Ra_{11} = 180\,290$ [i.e. Ra_{nl} for the $n=1$ 'even' ($l=1$) mode] is stable. In fact, computationally this branch is stable to as high a Rayleigh number as we considered, well beyond where quantitative accuracy of the approximation could be claimed. Experimentally, this pattern was observed at Rayleigh numbers of the order of $10\,Ra^c$ at this aspect ratio for $Pr=6{\cdot}7$ (Reference 7). The stable branches are so designated in the figure legend.

The approximate solutions represented by each branch are given by expansion (25). The archetypical spatial structure of a solution on a given branch is determined by the particular subset of the coefficients (F_{nl}) that are non-zero, and by their ordering in terms of magnitude, while the variation along a branch is determined by the changes in magnitude, both relative and absolute, of the coefficients in this subset. For example, the branches bifurcating from $\tilde{Ra}_{01}$, $\tilde{Ra}_{11}$ and $\tilde{Ra}_{21}$ are composed of the following subsets of (F_{nl}), represented in terms of the pairs (n, l):

branch bifurcating from $\tilde{Ra}_{01}$: $[(0,1),(0,2)]$,

branch bifurcating from $\tilde{Ra}_{11}$: $[(1,1),(0,2),(2,2)]$,

branch bifurcating from $\tilde{Ra}_{21}$: $[(2,1),(0,2)]$.

The contributing modes are listed (from left to right) in order of decreasing amplitude at a slightly supercritical Rayleigh number. Henceforth, these branches are denoted as follows: (0e, 0o) is used to denote the branch bifurcating from $\tilde{Ra}_{01}$ [since its approximation includes the $n=0$ 'even' and $n=0$ 'odd' linear stability solutions] (1e, 0o, 2o) the branch bifurcating from $\tilde{Ra}_{11}$, and (2e, 0o) the branch bifurcating from $\tilde{Ra}_{21}$. For each branch, all other coefficients F_{nl} are zero as computed. In

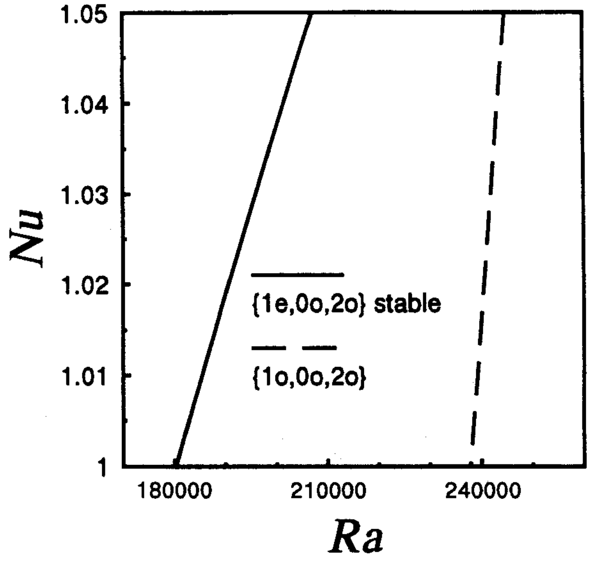

Figure 4. Bifurcation diagram for $\gamma=1/7$ with $Pr=6{\cdot}7$ (The modes that contribute to the description of each branch are shown in braces.)

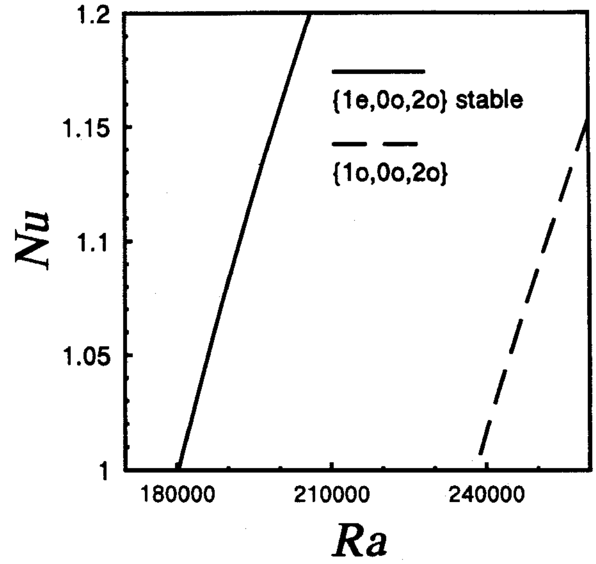

Figure 5. Bifurcation diagram for $\gamma=1/7$ with $Pr=0{\cdot}02$

addition, the set of non-zero coefficients used to describe the solution along each branch comprises a suitable set of coefficients (H_{jlt}). A similar bifurcation diagram for $Pr=0{\cdot}02$ is shown in Figure 5.

At an aspect ratio of $\gamma=1/2$, the critical mode for the onset of convection is again the $n=1$ even mode. The bifurcation diagram is shown in Figure 6. The critical Rayleigh number for the onset of convection is $Ra^c=Ra_{11}=3774$. The flow field corresponding to $Pr=6{\cdot}7$ at $Ra=4000$ is shown in

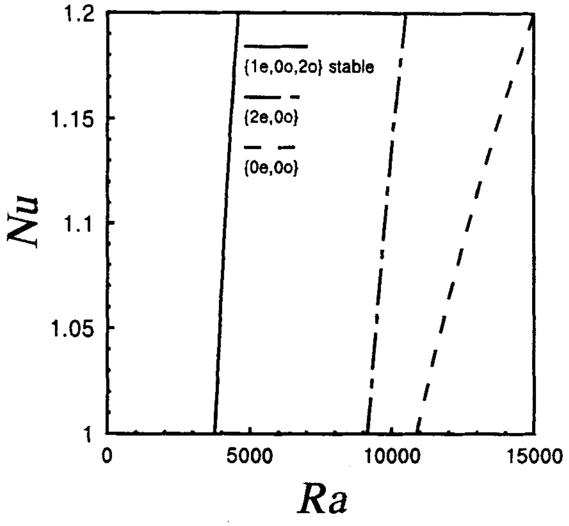

Figure 6. Bifurcation diagram for $\gamma = 1/2$ with $Pr = 6{\cdot}7$

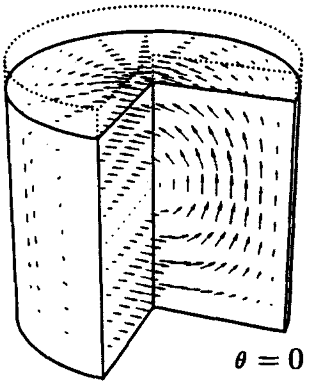

Figure 7. 3D perspective of flow at $Ra = 4000$ for $\gamma = 1/2$ with $Pr = 6{\cdot}7$ ($|\mathbf{u}|_{\max} = 0{\cdot}628$). (Dotted lines indicate location of the top of cylinder)

Figure 7. This flow has the character of nearly a 'pure' $n = 1$ mode in the sense that the secondary recirculations are very weak. This case served as a test of the numerical approximation, in that some quantitative information was available from two other individuals working on the mono-component problem, as summarized in Table I. In this table, $u_z^{\max}$ is the maximum vertical velocity and $u_r^{\max}$ is the maximum radial velocity. The agreement between the results of this work and the numerical results of Bontoux[12] is quite good, especially considering that two vastly different approximate solution techniques were used. (Both of the other analyses employed the finite difference method.) The disagreement in $u_z^{\max}$ is 4·3%, while that in $u_r^{\max}$ is only 1·5%. The maxima were found in the $\theta = 0$ plane. The agreement between these two works suggests a problem with that of Neumann.[13] In that latter work, the velocities appear to be roughly 50% too large, which also explains the greater Nusselt number found compared to this study. There are other indications of problems with the solutions presented in Reference 13, such as bifurcation

Table I. Comparisons of computational results for a cylinder with $\gamma=1/2$ and $Pr=6{\cdot}7$ at $Ra=4000$

Nu	$u_z^{\max}$	$u_r^{\max}$	Reference
1·15	6·1	5·1	Neumann[13]
—	4·40	3·23	Bontoux[12]
1·06	4·22	3·28	This paper

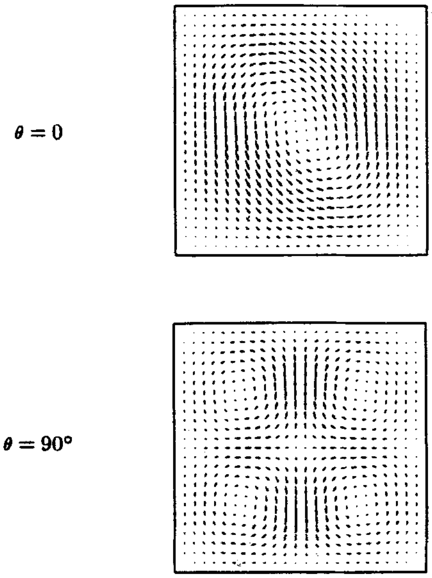

Figure 8. Flow profiles in the $\theta=0$ and $\theta=90°$ planes at $Ra=17\,500$ for $\gamma=1/2$ and $Pr=6{\cdot}7$ ($\theta=0$, $|\mathbf{u}|_{\max}=4{\cdot}73$; $\theta=90$, $|\mathbf{u}|_{\max}=1{\cdot}96$)

diagrams in which the solution branches show positive second derivatives of Nu with respect to Ra. The problem with that work may result from the conditions imposed on nodes along the centreline of the cylinder ($r=0$). The comparisons in Table I, although limited in scope, give credibility to the approximate solution technique used in this work.

Although it was speculative, we carried the calculations for the case of $\gamma=1/2$ and $Pr=6{\cdot}7$ up to $Ra=15\,000$, which is nearly $Ra=4\,Ra^c$. The results suggest that the (1e, 0o, 2o) branch is stable, while the (0e, 0o), and (2e, 0o) branches are unstable. Experimentally, Müller *et al.*[7] found flows similar to the (1e, 0o, 2o) branch to be stable beyond $Ra=10^5$. Qualitatively, the comparisons between the experimental and theoretical results are fairly good, but such qualitative comparisons of gross features provide a rather weak test of the accuracy of the numerical results. The results of Neumann,[13] which are apparently in error by nearly 50% in terms of the magnitude of the velocity field, also compare well qualitatively with the experimental results.

Continuing this somewhat speculative approach Figure 8 shows that the flow for $Pr=6{\cdot}7$ at $Ra=17\,500$ is tilted, yielding strong secondary recirculations. The secondary recirculations are already evident at $Ra=4000$ for the $Pr=0{\cdot}02$ case, which is presented in Figure 9, because of the larger non-dimensional velocities characteristic of the small Pr fluids. Similar flow structure was observed by Müller *et al.*[7] The bifurcation diagram for the low Prandtl number case is shown in Figure 10. The numerical results suggest that the (1e, 0o, 2o) branch becomes unstable at $Ra=13\,400$ (which, of course, is well past where this approximation could be expected to be accurate) with respect to a 3D (three-dimensional) oscillatory disturbance, while the experimental results of Müller *et al.*[7] on liquid gallium ($Pr\approx 0{\cdot}02$) show this branch to be stable to roughly four times this Rayleigh number. It seems probable that this disparity is caused by the accuracy of our approximation. However, interestingly, the experimental results of Müller *et al.*[7] show the $\gamma=1/2$ case at $Pr\approx 0{\cdot}02$ to be exceptional, in that they found the stationary flow regime to be stable to a Rayleigh number that is many more times the critical Rayleigh number for the onset of convection than at any other aspect ratio for which they presented data. No parallel behaviour was found for the onset of instability in their experiments on water. In fact, the theoretical

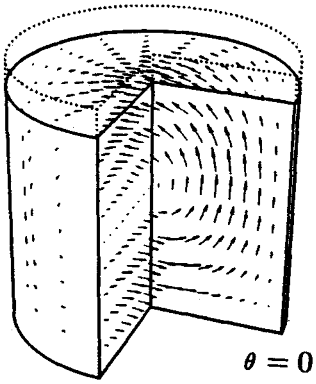

Figure 9. 3D perspective of flow at $Ra=4000$ for $\gamma=1/2$ with $Pr=0{\cdot}02$ ($|\mathbf{u}|_{\max}=33{\cdot}0$)

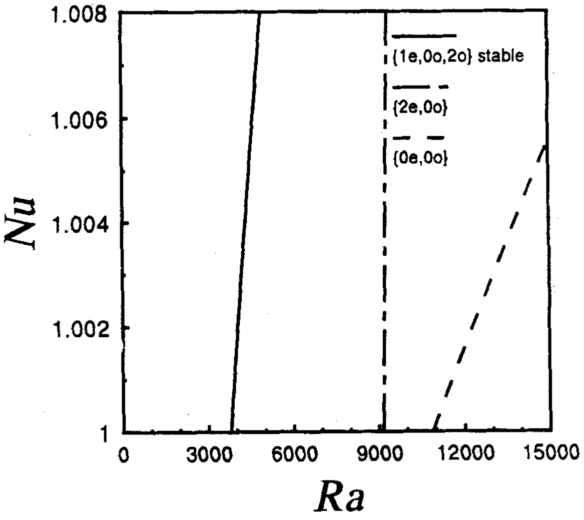

Figure 10. Bifurcation diagram for $\gamma=1/2$ with $Pr=0{\cdot}02$

prediction of the transition to a periodic state fits nicely on a smooth curve with the experimentally determined transition points shown at all other aspect ratios. It at least suggests that the $Pr = 0{\cdot}02$ case at $\gamma = 1/2$ should be investigated more carefully, both theoretically and experimentally.

At an aspect ratio of $\gamma = 1$, the bifurcation diagram for $Pr = 6{\cdot}7$ becomes more interesting, as seen in Figure 11. The critical Rayleigh number at this aspect ratio is $Ra = 2260$, and the critical flow state is axisymmetric, corresponding to the $n = 0$ even mode. A stable axisymmetric solution at $Ra = 2500$ is shown in Figure 12. (Note that using the Boussinesq approximation does not allow the theory to distinguish between the two possible solutions corresponding to either upflow or downflow at the centre of the cylinder. In order to determine this, the temperature dependence of some physical property other than the linear density variation in the buoyancy term must be accounted for.) However, the axisymmetric branch becomes unstable at $Ra = 2850$ with respect to a stationary disturbance with a spatial dependence corresponding to $n = 2$. The result is a new stable solution that is characterized by the following set of non-zero coefficients (F_{nl}) for the

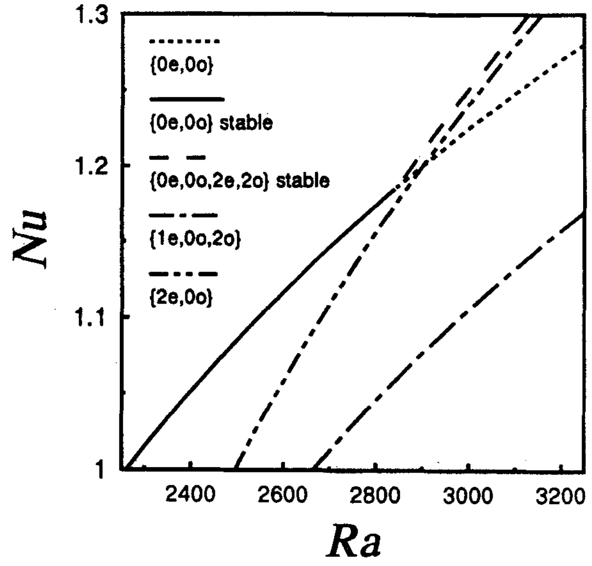

Figure 11. Bifurcation diagram for $\gamma = 1$ with $Pr = 6{\cdot}7$

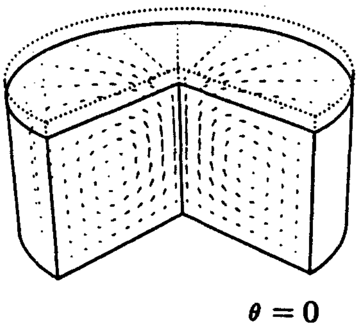

Figure 12. 3D perspective of flow at $Ra = 2500$ for $\gamma = 1$ with $Pr = 6{\cdot}7$ ($|\mathbf{u}|_{\max} = 1{\cdot}14$)

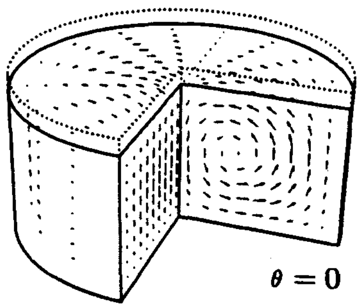

Figure 13. 3D perspective of flow at $Ra=4000$ for $\gamma=1$ with $Pr=6{\cdot}7$ ($|\mathbf{u}|_{\max}=2{\cdot}17$)

multidimensional part of expansion (25), represented in terms of the pairs (n, l):

$$\text{secondary branch bifurcating from (0e, 0o): } [(0, 1), (0, 2), (2, 1), (2, 2)]. \qquad (33)$$

Henceforth, this branch is denoted by (0e, 0o, 2e, 2o). A solution on this secondary branch at $Ra=4000$ is shown in Figure 13. This solution consists of two adjacent counter-rotating rolls, each filling half the cylinder. The numerical result that a new solution supersedes the axisymmetric solution at $Ra=2850$ for $\gamma=1$ disagrees with the experimental findings of Müller *et al.*,[7] who apparently found axisymmetric flows in water at Rayleigh numbers well past $Ra=10^4$. However, using a cylinder with a transparent lid, Stork and Müller[14] observed a flow near the onset of convection in a silicon oil with a planform corresponding to the (0e, 0o, 2e, 2o) branch in a cylinder with $\gamma=0{\cdot}8$, although its stability was questionable at that aspect ratio. Furthermore, the (0e, 0o, 2e, 2o) solution would be very hard to distinguish from an axisymmetric flow using the vertical light cut technique employed by Müller *et al.*,[7] since a vertical light cut would have to be made in a small range of angles in order to detect the non-axisymmetry of the (0e, 0o, 2e, 2o) type flow. Vertical light cuts at any other angles would look essentially 'axisymmetric'. In their experiments no possibility existed for the visualization of horizontal light cuts since the top and bottom of the container were copper. In addition, it would be possible to bias the experiment arbitrarily toward an axisymmetric solution by imperfections introduced in order to allow for thermal expansion of the liquid in the apparatus, as noted by Stork and Müller.[14] This disagreement must be examined more carefully.

The bifurcation diagram for $Pr=0{\cdot}02$ at $\gamma=1$ is shown in Figure 14. For this low Prandtl number case, it is seen that the axisymmetric solution becomes unstable with respect to the (0e, 0o, 2e, 2o) solution at a very low Rayleigh number, $Ra=2430$, for $Pr=0{\cdot}02$. Flow solutions along this secondary branch look very much like that shown in Figure 13 for $Pr=6{\cdot}7$, except that slightly more inertia is evident in the lower Prandtl number flows at the same Rayleigh number.

The next aspect ratio considered is $\gamma=1{\cdot}57485=\gamma_D$, which yields a numerical double eigenvalue of the linear stability problem, corresponding to the crossing of the $n=0$ and $n=1$ marginal stability limits shown in Figure 10 of Part I; the Rayleigh numbers Ra_{01} and Ra_{11} corresponding to the $n=0$ even and $n=1$ even modes differ in the 14th significant figure (for the number of trial functions used to generate the linear stability solutions that are employed in the approximate solution of the non-linear problem). This aspect ratio is termed γ_D for convenience and represents a co-dimension two bifurcation[15] (i.e., γ_D is a double eigenvalue of index 1). Since these two modal solutions have the same Rayleigh number, linear stability theory cannot predict the spatial form of even the feeblest flow. The bifurcation diagram for $Pr=6{\cdot}7$ is shown in Figure 15. Both the (0e, 0o) and (1e, 0o, 2o) branches bifurcate from $Ra=1914$, but the axisymmetric branch is

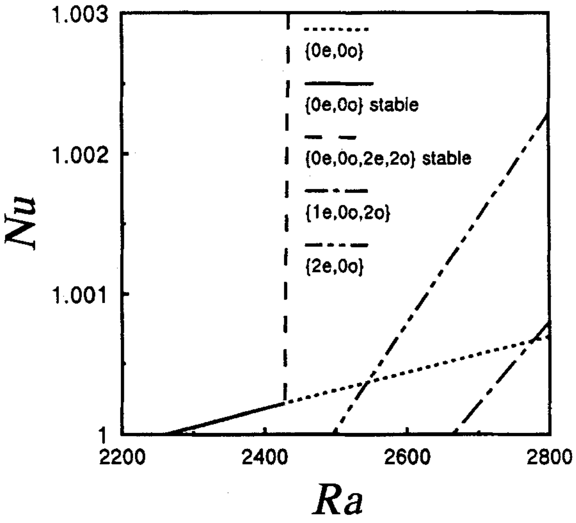

Figure 14. Bifurcation diagram for $\gamma=1$ with $Pr=0{\cdot}02$

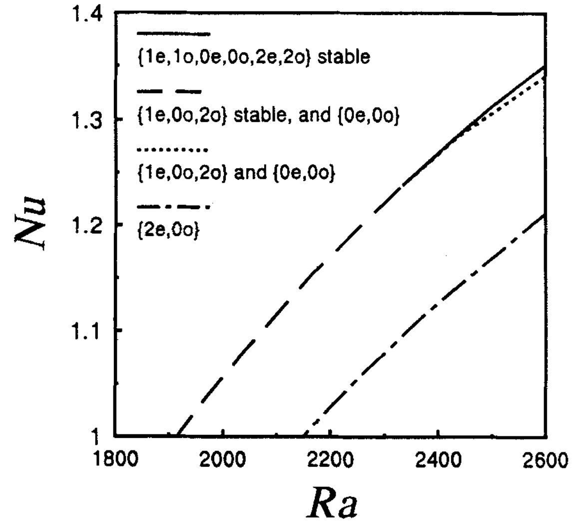

Figure 15. Bifurcation diagram for $\gamma=1{\cdot}57485$ with $Pr=6{\cdot}7$

unstable at the outset. These branches follow nearly identical trajectories in the *Nu* versus *Ra* plane. Consequently, they appear superimposed in Figure 15. The stable (1e, 0o, 2o) solution at $Ra=2000$ is shown in Figure 16. This solution consists of three adjacent, counter-rotating rolls, with the middle possessing the strongest flow, as expected. The middle roll extends to the sidewalls in the $\theta=90°$ plane, although the flow is much stronger toward the centre of the cylinder. The horizontal planform of this solution is better seen in Figure 17, which illustrates the vertical velocity field at $z=0$ for the flow shown in Figure 16; the view in Figure 17 is from almost 180° to the rear relative to that in Figure 16. In appearance, the temperature field at $z=0$ is almost

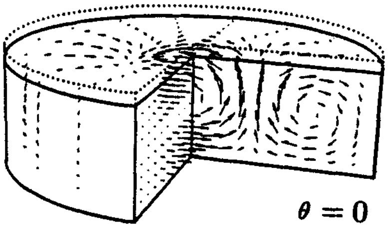

Figure 16. 3D perspective of flow at $Ra = 2000$ for $\gamma = 1{\cdot}57485$ with $Pr = 6{\cdot}7$ ($|\mathbf{u}|_{\max} = 0{\cdot}790$)

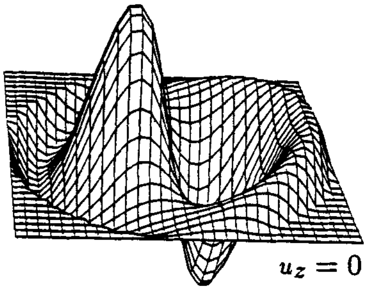

Figure 17. Vertical velocity field at $z = 0$ for $Ra = 2000$ for $\gamma = 1{\cdot}5748$ with $Pr = 6{\cdot}7$; the view is from the rear of the previous figure

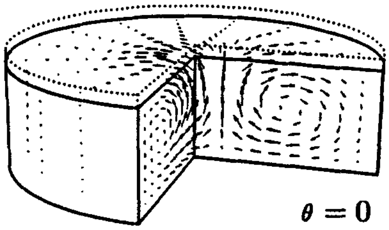

Figure 18. 3D perspective of flow at $Ra = 4000$ for $\gamma = 1{\cdot}57485$ with $Pr = 6{\cdot}7$ ($|\mathbf{u}|_{\max} = 4{\cdot}69$)

indistinguishable from the vertical velocity field, as expected. This branch becomes unstable with respect to a multimode disturbance at $Ra = 2330$, so that the resulting solution contains non-zero amplitude coefficients for all six of the linear stability eigenvectors used to expand the non-linear solution in the form of expansion (25), and is appropriately denoted by (1e, 1o, 0e, 0o, 2e, 2o), which represents a stable mixed mode solution. This latter branch is stable, and it is represented by the uppermost curve in Figure 15. Initially, the flow solutions along this branch look very much like a (1e, 0o, 2o) solution. As Ra is increased, one of the side rolls grows at the expense of the other two rolls, (as seen in Figure 18) which shows the solution at $Ra = 4000$ on this branch. Stork and Müller[14] observed a similar flow near the onset of convection in a flow visualization experiment using a silicon oil. In both the theoretical and experimental flow visualizations, the flow on one side of the cylinder forms a more or less closed, toroidal structure, while the flow on the other side curves nearly halfway around the cylinder. While the qualitative features of this

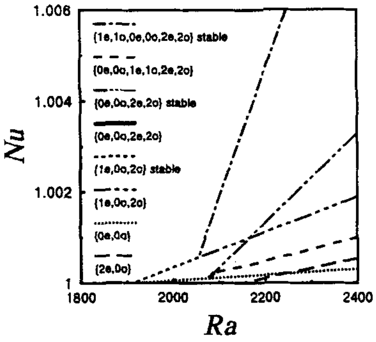

Figure 19. Bifurcation diagram for $\gamma=1{\cdot}57485$ with $Pr=0{\cdot}02$

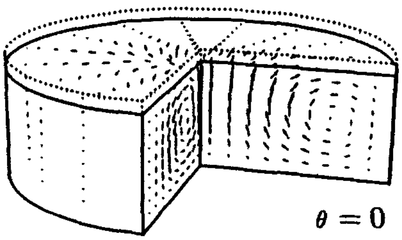

Figure 20. 3D perspective of flow at $Ra=2100$ for $\gamma=1{\cdot}57485$ with $Pr=0{\cdot}02$ ($|\mathbf{u}|_{\max}=21{\cdot}2$)

flow seem physically reasonable, the quantitative aspects of this solution should be regarded as speculative because of the truncated nature of our solution representation.

The bifurcation diagram for $Pr=0{\cdot}02$ and $\gamma=\gamma_D$ is shown in Figure 19. For the $Pr=0{\cdot}02$ case, the stable (1e, 1o, 0e, 0o, 2e, 2o) branch bifurcates from the (1e, 0o, 2o) branch at $Ra=2056$. The (0e, 0o, 2e, 2o) branch bifurcates from the unstable axisymmetric (0e, 0o) branch at $Ra=2077$, but is unstable itself until $Ra=2090$. At $Ra=2090$, an unstable (0e, 0o, 1e, 1o, 2e, 2o) branch bifurcates from the (0e, 0o, 2e, 2o) branch. (All of the bifurcations analogous to those of the $Pr=6{\cdot}7$ case occur at lower Rayleigh numbers for $Pr=0{\cdot}02$ than for $Pr=6{\cdot}7$.) Figure 20 shows a solution at $Ra=2100$ on the (0e, 0o, 2e, 2o) branch. The recirculations in the $\theta=90°$ plane have tilted, driving a strong upflow in the centre of the cylinder.

Near $\gamma=1{\cdot}8$, the $n=1$ even mode is clearly the critical mode, but only for a relatively small range of aspect ratio. For $\gamma>\gamma_D$, the critical mode changes often as γ is increased. This behaviour results from the sidewall influence (or lack thereof) on the flow structure (see Reference 3). Consequently, this is a region of particular interest for a weakly non-linear study in order to determine how these features, already apparent in the linear stability results, affect a finite amplitude solution near Ra^c.

It is known from Part I that at $\gamma=2{\cdot}06$, the modal Rayleigh numbers Ra_{01}, Ra_{11} and Ra_{21} for the $n=0$, $n=1$ and $n=2$ modes, respectively, are all very close in magnitude, with $n=2$ being the critical mode. The actual values are $Ra_{21}=1834$, $Ra_{11}=1837$ and $Ra_{01}=1839$. Consequently, it is very difficult to forecast the finite amplitude behaviour at this aspect ratio from the linear stability results. Interestingly, the bifurcation diagrams for $Pr=6{\cdot}7$ and $Pr=0{\cdot}02$, which are given in Figures 21 and 22, respectively, are both quite simple. In both cases, the (2e, 0o) branch is stable

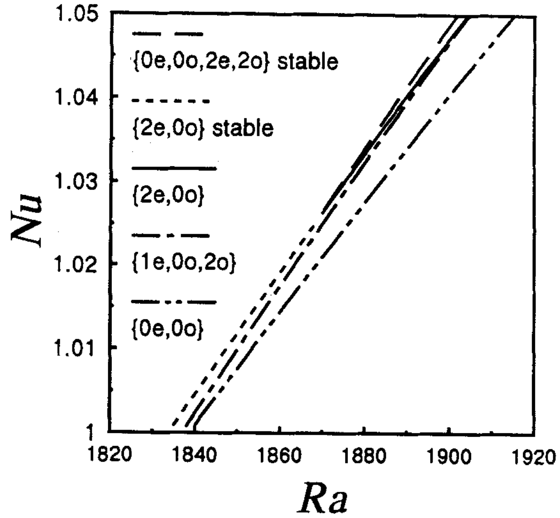

Figure 21. Bifurcation diagram for $\gamma=2{\cdot}06$ with $Pr=6{\cdot}7$

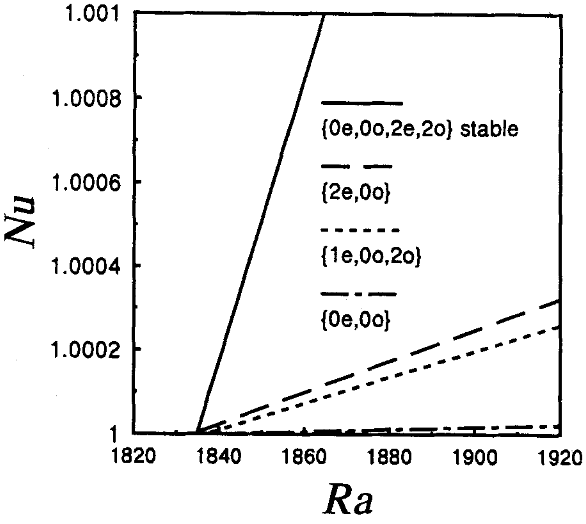

Figure 22. Bifurcation diagram for $\gamma=2{\cdot}06$ with $Pr=0{\cdot}02$

initially, but goes unstable almost immediately with respect to a (0e, 0o, 2e, 2o) branch. For $Pr=6{\cdot}7$ this occurs at $Ra=1869$, while at $Pr=0{\cdot}02$ it occurs at $Ra=1835$. For the $Pr=0{\cdot}02$ case, the (0e, 0o, 2e, 2o) branch becomes unstable to oscillatory disturbances at $Ra=2810$. Figure 23 displays a solution at $Ra=1850$ for $Pr=6{\cdot}7$ on the stable (2e, 0o) branch, near the onset of convection. At this aspect ratio there are multiple rolls across the diameter in both the $\theta=0°$ and $\theta=90°$ planes. The flow is very 3D, with the basic planform being up, down, up, down moving 360° around the cylinder at a fixed radius. The flow essentially circulates around axes at $z=0$ in the $\theta=\pm45°$ planes, with the $\theta=0°$ and $\theta=90°$ planes, which are shown in Figure 23, serving as

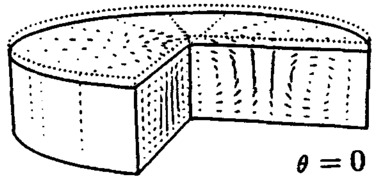

Figure 23. 3D perspective of flow at $Ra=1850$ for $\gamma=2{\cdot}06$ with $Pr=6{\cdot}7$ ($|\mathbf{u}|_{\max}=0{\cdot}324$)

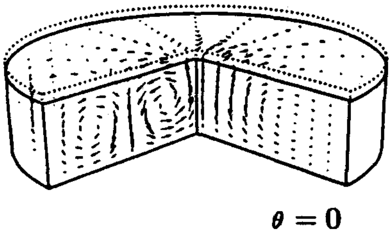

Figure 24. 3D perspective of flow at $Ra=2500$ for $\gamma=2{\cdot}06$ with $Pr=6{\cdot}7$ ($|\mathbf{u}|_{\max}=2{\cdot}73$)

azimuthal dividing planes for the recirculations. The regions of strongest upflow and downflow are also located in the $\theta=0°$ and $\theta=90°$ planes. (The reader is cautioned against attempting to envision 2D continuity constraints, since the flow is very 3D.) A flow solution for $Pr=6{\cdot}7$ at $Ra=2500$ on the (0e, 0o, 2e, 2o) branch is shown in Figure 24. This solution strongly resembles a flow pattern observed by Stork and Müller[14] near the onset of convection in silicon oil in a cylinder with $\gamma=2$. In particular, both the experimental and theoretical flow visualizations show horizontal planforms with a somewhat elongated toroidal structure in the centre of the cylinder.

Binary fluid mixtures

A cylinder aspect ratio of $\gamma=\gamma_D$ yields a numerical double eigenvalue of the linear stability problem for a monocomponent fluid. It is interesting to see how the convective behaviour is changed by the introduction of a small amount of Soret diffusion. First, it is appropriate to consider the modal stability threshold as a function of ψ (for $\zeta=0$) at this aspect ratio, which is displayed in Figure 25. For $\psi<1{\cdot}5$, the axisymmetric ($n=0$) mode is seen to be the critical mode, while for larger ψ, the antisymmetric ($n=1$) mode is the critical mode. Neglecting the Dufour effect (i.e. for $\zeta=0$), the physical parameters for a mixture of xenon and argon with a xenon mole fraction of $X_{\mathrm{Xe}}=0{\cdot}2$ are $\psi=0{\cdot}06$, $\tilde{P}r=0{\cdot}71$ and $\tilde{S}c=1{\cdot}1$. (The ψ value was obtained from Abernathey and Rosenberger.[16] The Prandtl and Schmidt numbers were estimated from data available in Touloukian.[17]) At $\gamma=\gamma_D$ for this ψ, the $n=0$ mode is the critical mode, with the $n=1$ mode having the next lowest modal Rayleigh number. Specifically, $\tilde{R}a_{01}=1721$, and $\tilde{R}a_{11}=1760$. The bifurcation diagram for this case is given in Figure 26 over the range $1700\leqslant\tilde{R}a\leqslant2000$. Initially, the axisymmetric (0e, 0o) branch is stable, as expected on the basis of the linear stability theory. A solution at $\tilde{R}a=1800$ on this branch is shown in Figure 27. For comparison, recall that for the monocomponent case, the critical Rayleigh number at $\gamma=\gamma_D$ is $\tilde{R}a=Ra=1914$, and the flow at onset is antisymmetric, despite the fact that $Ra_{01}=Ra_{11}$. From Figure 26, it can be seen that the axisymmetric branch becomes unstable at $Ra=1890$, just beyond where it crosses the unstable (1e, 0o, 2o) branch, and still at a lower Rayleigh number than the critical value for the

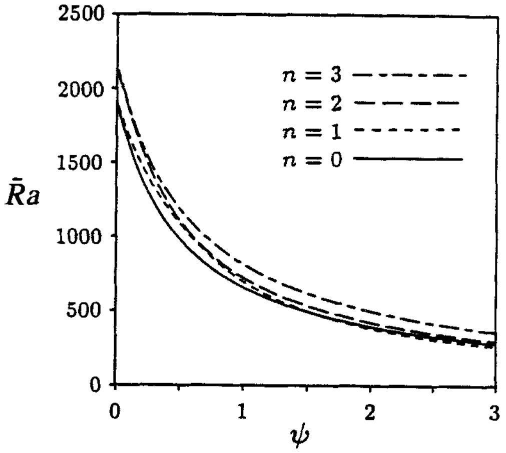

Figure 25. Critical Rayleigh number as a function of ψ for $0 \leqslant \psi \leqslant 3$ with $\gamma = 1{\cdot}57485$

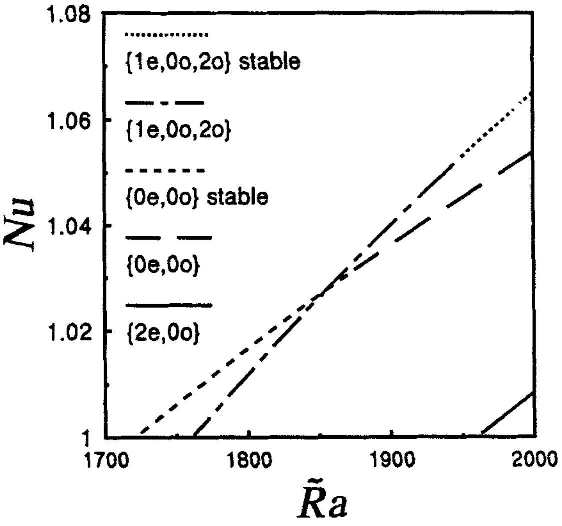

Figure 26. Bifurcation diagram for $\gamma = 1{\cdot}57485$ for an Xe–Ar mixture with $X_{\mathrm{Xe}} = 0{\cdot}2$ ($\psi = 0{\cdot}06$)

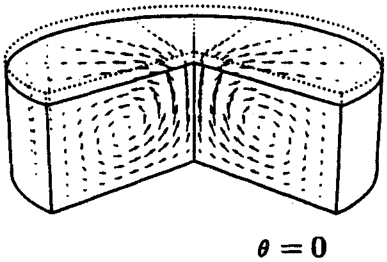

Figure 27. 3D perspective of flow at $\tilde{R}a = 1800$ for $\gamma = 1{\cdot}5748$ for Xe–Ar with $X_{\mathrm{Xe}} = 0{\cdot}2$ ($\psi = 0{\cdot}06$) ($|\mathbf{u}|_{\max} = 5{\cdot}46$)

onset of convection for the monocomponent case. It seems probable that the instability of this branch must be triggered by the bifurcation of a secondary branch from it, but no such branch was found. Interestingly, the disturbance that triggers this instability is antisymmetric in form, which foreshadows the behaviour of the antisymmetric branch. It is also worth noting that the (0e, 0o, 2e, 2o) branch does not bifurcate from the axisymmetric branch until $\tilde{Ra}=2008$, and is unstable to as high a Rayleigh number as the analysis is carried. In contrast, the (0e, 0o, 2e, 2o) branch eventually became stable for the monocomponent case. As in the monocomponent case, the (2e, 0o) branch is unstable over the entire range of Rayleigh numbers considered.

The (1e, 0o, 2o) branch is initially unstable, but becomes stable at $\tilde{Ra}=1940$, not long after the (0e, 0o) branch becomes unstable to an antisymmetric disturbance. A solution at $\tilde{Ra}=2000$ on this branch is shown in Figure 28, and appears to be quite comparable to the solution shown in Figure 16, at $Ra=2000$ on the analogous branch for the monocomponent case for $\gamma=\gamma_D$. Again, it seems likely that this change in stability of the (1e, 0o, 2o) branch signals the bifurcation of a secondary branch, but no such branch was found. (As pointed out by a reviewer, this implies that this point represents a non-simple bifurcation point[15] or the inability of our numerical scheme to converge to the solution.) In addition, the (1e, 0o, 2o) branch is found to become unstable at $\tilde{Ra}=2570$, but no secondary bifurcation was found there either. In both of these cases, it is apparent from the algebraic equations for the amplitude coefficients that if these secondary branches were to be described by expansion (25), they would probably be represented by solutions with non-zero coefficients for all six modes. The difficulty in finding these new branches points out the major difficulty with this technique: once one solution has been found on a particular branch, the entire branch is then easily tracked by the use of a first-order continuation scheme, but there is no prescription for finding that first solution. This proved to be a general difficulty for the study of binary fluid systems, probably as a result of the increased complexity of the non-linear algebraic equations for the amplitude coefficients. A possible remedy for this problem is the use of a homotopy continuation method,[18] but this capability has not been implemented for this study at the current time.

Water–methanol systems can exhibit substantial Soret effects. For a water–methanol mixture with a water weight fraction of $W_{H_2O}=0{\cdot}715$, the Soret coefficient is $\psi=1{\cdot}9$, and the Prandtl and Schmidt numbers are $\tilde{Pr}=9{\cdot}29$ and $\tilde{Sc}=820$.[19] From Part I it is known that the $n=0$ mode is the critical mode for this case with $\gamma=1{\cdot}8$. At approximately $\psi=2{\cdot}16$ for $\gamma=1{\cdot}8$, there is a double eigenvalue of the linear stability problem, and for greater ψ the $n=1$ mode is the critical mode. At $\psi=1{\cdot}9$ for $\gamma=1{\cdot}8$, $\tilde{Ra}_{01}=390{\cdot}1$ and $\tilde{Ra}_{11}=394{\cdot}9$, which is a rather small separation in Rayleigh number. The results that were found for $\gamma=\gamma_D$ with $\psi=0$, which is a double eigenvalue of the linear stability problem, and for $\psi=0{\cdot}06$ (i.e. the Xe–Ar mixture just discussed), a small deviation in ψ from the double eigenvalue, showed that the branch structure was fairly complicated in the neighbourhood of the double eigenvalue. Based on analogy with that behaviour, one might

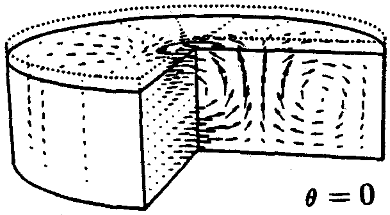

Figure 28. 3D perspective of flow at $\tilde{Ra}=2000$ for $\gamma=1{\cdot}5748$ for Xe–Ar with $X_{Xe}=0{\cdot}2$ ($\psi=0{\cdot}06$) ($|\mathbf{u}|_{max}=8{\cdot}22$)

expect the bifurcation diagram for the methanol–water system with $\psi = 1{\cdot}9$ to be rather complex. In addition, a consideration of the modal stability limits as a function of aspect ratio at $\psi = 2{\cdot}16$, which are displayed in Figure 29, supports this expectation. Surprisingly, this is not the case: the bifurcation diagram is quite uneventful, showing the (0e, 0o) branch to be stable over the entire range of Rayleigh numbers considered, while the (1e, 0o, 2o) and (2e, 0o) branches are always unstable over this range. In addition, the Nusselt numbers are observed to be extremely small, suggesting that the convective heat transport is weak. Figure 30 shows a flow solution at $Ra = 500$ along the stable axisymmetric branch. The flow consists of a single toroidal roll and is quite weak, with a maximum dimensionless velocity of $|\mathbf{u}|_{\max} = 0{\cdot}0097$, even though this Rayleigh number is nearly 30% greater than the critical value of $\tilde{Ra}^c = 390{\cdot}1$ for the onset of convection. This result supports the observation for the Xe–Ar mixture that the incipient flow resulting from the increased destabilization provided by the Soret effect is relatively weak. Moreover, the conclusion that the incipient flow caused by the enhanced destabilization resulting from the Soret effect is relatively weak is in agreement with experimental observations. Hurle and Jakeman[19] conducted a careful series of experiments measuring the heat flux through shallow layers of water–methanol mixtures with comparable Soret coefficients to the system studied here. They were unable to detect the onset of convection until their systems had attained approximately the classical Bénard stability limit of $Ra = 1708$ for a monocomponent fluid. Based on the results of the present analysis, this is not hard to understand, considering the extremely small Nusselt numbers for the

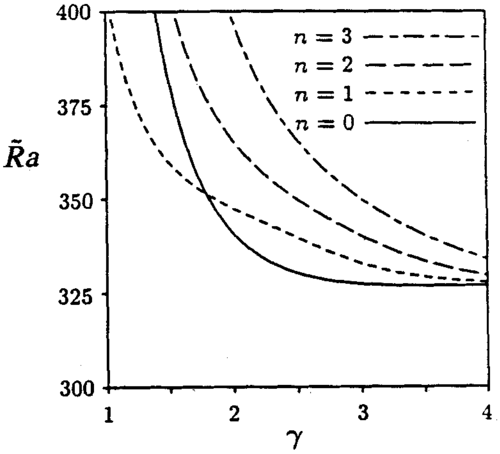

Figure 29. Critical Rayleigh number as a function of aspect ratio for $1 \leqslant \gamma \leqslant 4$ with $\psi = 2{\cdot}16$

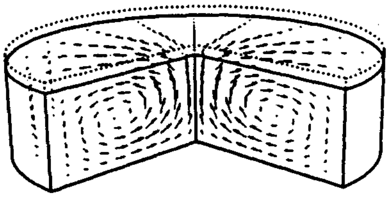

Figure 30. 3D perspective of flow at $\tilde{Ra} = 500$ for $\gamma = 1{\cdot}8$ for water–methanol with $W_{H_2O} = 0{\cdot}715$ ($\psi = 1{\cdot}9$) ($|\mathbf{u}|_{\max} = 0{\cdot}00965$)

$\psi = 1{\cdot}9$ case. As pointed out by Hurle and Jakeman, the reason for this is that '. . . convection can only be driven at a rate which is commensurate with the maintenance of a solute gradient by the Soret effect'. A more vigorous flow would tend to destroy the driving force for convection. The establishment of a concentration gradient in the system is essentially a secondary effect in this problem, resulting from the applied temperature gradient. Consequently, the concentration difference between the top and bottom of the cylinder is not fixed. A clear illustration of this is provided in Figure 31, which displays the horizontally averaged temperature and concentration fields corresponding to the flow solution shown in Figure 30. The fact that the temperature and concentration gradients have opposite signs results from the fact that the Soret effect causes water, which is the denser substance, to migrate to the cold, upper boundary. (Water is chosen as substance 'one' here.) The horizontally averaged temperature field is essentially unaffected by the flow, while the horizontally averaged concentration field is slightly distorted, and the concentration difference between the top and bottom of the cylinder is diminished from that of the critical state for the onset of convection (which is represented by the corners of the figure). (Note that because of the Soret effect, the concentration gradient normal to the top and bottom of the cylinder must be non-zero in order to satisfy the boundary conditions of zero mass flux through the top and bottom.) The concentration variable plotted here results from a rescaling of the dimensionless variables of the problem in order to subtract the temperature field from the η-field. The variable that is plotted is

$$W^{R} \equiv \frac{1}{\tilde{Ra}}(\tilde{Sc}\,\eta - \tilde{Pr}\,T) + z,$$

where $T = \bar{T} + \hat{T}$ is the dimensionless temperature, and z is the dimensionless vertical co-ordinate. This can be rewritten as

$$W^{R} = \frac{(W_1 - \bar{W}_1)}{(W^{c}_{1_T} - W^{c}_{1_B})},$$

where $\bar{W}_1 = \frac{1}{2}(W^{c}_{1_T} + W^{c}_{1_B})$, and $W^{c}_{1_T}$ and $W^{c}_{1_B}$ are the mass fractions of substance 1 at the top and bottom of the cylinder, respectively, for the corresponding (unstable) conduction state at the same Rayleigh number. This variable then gives a measure of the distortion of the concentration field (in terms of mass fraction) relative to the linear field for the conduction state. From the figure it is clear that the horizontally averaged solute gradient is in fact appreciably weakened by the mild flow.

What all of this points to is a fundamental difference between the monocomponent case and the binary case in the mechanisms that trigger the loss of stability of the conduction state. For the monocomponent case, flow occurs when enough potential energy has been stored in the density field so that it can be converted into kinetic energy faster than it can be dissipated by viscosity and

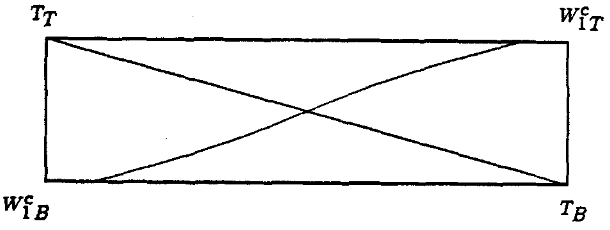

Figure 31. Horizontally averaged temperature and concentration fields for water–methanol with $W_{H_2O} = 0{\cdot}715$ ($\psi = 1{\cdot}9$)

the stabilizing influence of conduction. The additional contribution driving the instability in a binary mixture is the potential energy stored in the concentration field. In contrast to conduction, mass diffusion, which plays an important role in binary systems, typically acts on a much longer time scale (at least for liquids), as can be seen by comparing the Prandtl and Schmidt numbers for a given fluid. This means that a perturbation in concentration is typically dissipated much more slowly than a thermal perturbation. Consequently, even though the concentration field is essentially a secondary effect resulting from Soret diffusion driven by the applied temperature field for the current problem, concentration effects can substantially decrease the stability of a fluid mixture. As a result of the longer time scale for diffusion relative to conduction, the minimum potential energy gradient required to drive flow in the binary case is reduced relative to the monocomponent case, resulting in relatively lower velocities near the onset of convection in a binary fluid. Although this secondary mechanism in the binary case can be destabilizing in terms of diminishing the threshold for the onset of convection, it is fragile, and is easily destroyed by flow. For the weak flow shown in Figure 30, the difference in the horizontally averaged weight fraction from top to bottom in the cylinder is reduced to 82% of that for the corresponding conduction state.

A matter that is very important to crystal growers is the formation of lateral concentration gradients in an ampoule in which a crystal is being grown. While the velocity clearly goes to zero at the cylinder sidewall, as required, the downflow (upflow) near the wall lowers (raises) the temperature at the sidewall relative to the linear, conduction profile. The concentration field is similar to the temperature field, but is inverted. The reason for this is that water, which is substance 1 here, tends to concentrate in the colder fluid as a result of the Soret effect. For the flow shown in Figure 30, at $z=0$ the maximum vertical velocity is $u_{z_{max}}=0{\cdot}0097$, the maximum temperature is $T^{R}_{max}=0{\cdot}0023$, and the maximum concentration is $|W_1^R|_{max}=0{\cdot}38$. Each of these maxima occurs at $r=0$. Although the deviation of the temperature field from the value of $T^{R}=0$ at $z=0$ for the conduction state is small, as a result of the slow flow speed, the deviation of the concentration field from the value of $W_1^R=0$ at $z=0$ at the conduction state is sizeable. Hence, even though the overall concentration difference across the system would normally be small, the lateral inhomogeneity is large on that scale, being on the order of half the difference from top to bottom at the conduction state. Consequently, although the velocities are generally of small magnitude for flow in a binary system prior to achieving the critical Rayleigh number for a monocomponent fluid, they can, nonetheless, create relatively large lateral inhomogeneities in concentration. This is important, since it can be very damaging to the desired physical properties of the resulting crystal.

To illustrate how strongly the lateral inhomogeneities persist over the height of the cylinder, compare the perturbations in the velocity, temperature, and concentration fields at $z=0{\cdot}4$ (i.e. near the top, which is at $z=0{\cdot}5$) for the flow shown in Figure 30. At this height, the maximum velocity (perturbation) is quite small, being about one-tenth the magnitude of the maximum at $z=0$. Correspondingly, the temperature field is essentially flat, with a maximum value that is very nearly equal to the value at $z=0{\cdot}4$ for the conduction state. Nonetheless, the deviation of the concentration field from the value of $W_1^R=0{\cdot}4$ for the conduction state is again substantial, with a deep depression around $r=0$, the minimum of which has a value of $W_1^R=0{\cdot}014$. Thus, the concentration variation at $z=0{\cdot}4$, near the end of the container, is nearly 80% of that at $z=0$. This behaviour, in addition to having important consequences for growing crystals, also suggests that the tendency of the fluid to resist equilibration in concentration relative to temperature when ψ is larger causes the fluid to tend to retain its relative buoyancy longer in this case. Consequently, when ψ is larger, the fluid must traverse a relatively longer path along the top or bottom of the container (in terms of horizontal distance relative to the depth of the fluid) before its density is sufficiently altered to change the sign of its buoyancy leading to fewer, wider roll cells when ψ is larger.

One last binary system is now considered: a mixture of liquid tin and lead with $W_{\mathrm{Pb}}=0{\cdot}64$. This system is chosen because it is the one liquid–metal system for which a Soret coefficient was found that might be reliable; all other values that were found were measured in a regime in which flow was likely, rendering the data questionable. The value of the Soret coefficient for this system was computed from data given by Winter and Drickamer[20] and is huge: $\psi = 2800$. Recall from the definition of ψ with $\zeta=0$,

$$\psi=\frac{\kappa}{D}\left(\frac{S}{1+S}\right),$$

where S is the Soret separation number. Thus, the reason that ψ is so large is that κ/D is very large for liquid metals; here, $\kappa/D=3600$. (The physical properties used for this system, other than the Soret coefficient, were obtained from data given by Corriell *et al.*,[21] and are actually for small amounts of tin in lead. Although this does not correspond to the concentration at which the Soret coefficient data were available, it is hoped, nonetheless, that the resulting assemblage of physical properties will be representative of liquid–metal systems in at least a general sense.) The critical Rayleigh number for the onset of convection in this case is tiny: $\tilde{R}a^{c}=\tilde{R}a_{11}=0{\cdot}2906$, with the antisymmetric ($n=1$) mode being the critical mode. The next lowest modal Rayleigh numbers belong to the $n=0$ and $n=2$ modes, with $\tilde{R}a_{01}=0{\cdot}3251$ and $\tilde{R}a_{21}=0{\cdot}3363$. The Nusselt numbers near the onset of convection are so small that the bifurcation diagram is not presented; the heat transfer across the system is insignificant. With convection being so slight, it seems unlikely that significant non-linear behaviour could be found near the onset of convection. Consequently, this opportunity is taken to push the approximation well beyond its recommended limit of accuracy, to $\tilde{R}a=3$, which is about ten times the critical value. The (1e, 0o, 2o) branch is still found to be stable at this Rayleigh number. The corresponding flow field is shown in Figure 32. For this case, one essentially antisymmetric roll fills the cylinder, and no sign of substantial inertia is present. The maximum velocity magnitude is located at $r=0$ in the $\theta=0$ plane, about one-fifth of the height from either the top or the bottom of the cylinder, and is essentially horizontal. The magnitude is $|\mathbf{u}|_{\max}=0{\cdot}32$. The maximum vertical velocity is $|u_z|_{\max}=0{\cdot}12$, which is roughly one-third the global maximum velocity, and occurs at about $r=0{\cdot}6$. The temperature and concentration fields at the cylinder sidewall are offset from the zero value as a result of upflow or downflow near the wall, but in both cases the gradient at the sidewall is zero, as required. The maximum temperature deviation from the level of the linear, conduction field is only 2×10^{-5}, which is consistent with the small Rayleigh number. Although the absolute magnitude of the variation in concentration from top to bottom in the cylinder is undoubtedly small, the relative magnitude of the lateral deviation is substantial, showing a maximum deviation from peak to

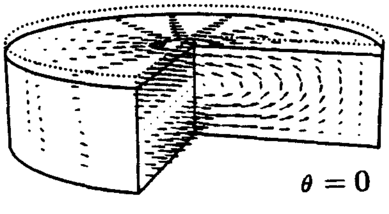

Figure 32. 3D perspective of flow at $\tilde{R}a=3$ for $\gamma=1{\cdot}8$ for lead–tin with $W_{\mathrm{Pb}}=0{\cdot}64$ ($\psi=0{\cdot}2800$) ($|\mathbf{u}|_{\max}=0{\cdot}322$)

trough of about 76% of the total deviation from top to bottom for the corresponding conduction state. The maximum concentration deviation occurs relatively close to the wall, at $r=0{\cdot}87$. This supports the conclusion that although the velocities resulting from the destabilization provided by the Soret effect are small, the resulting concentration effects can be important.

CONCLUSIONS

The cost and effort of generating a solution of the form of expansion (7) increase rapidly as the number of terms is increased. From a practical point of view, this is what limits the scope of this technique to a small range in Rayleigh numbers near the critical value for the onset of convection. Nonetheless, in this range, this technique was found to be very cost-effective relative to the alternative of using *local* approximation techniques such as the finite element or finite difference methods. Once the integrals in equations (19) and (20) have been evaluated for a particular cylinder aspect ratio (γ), and particular values of ψ and ζ, the Rayleigh, Prandtl and Schmidt numbers may be varied at very little cost. All that need be solved for each new set of values of ($\tilde{Ra}$, $\tilde{Pr}$, $\tilde{Sc}$) is a system of non-linear algebraic equations. In contrast, a new solution is required for each set of values of ($\tilde{Ra}$, $\tilde{Pr}$, $\tilde{Sc}$, ψ, ζ) if a local scheme is used. Although previous solutions may provide good initial guesses for a local scheme, the iterative approximate solution of the large number of nodal equations that would be required for a solution to a 3D problem such as this would be far more costly than the much smaller number of equations encountered here. Moreover, the Rayleigh number range for which a weakly non-linear approach is appropriate is precisely the range in which a local solution technique is least efficient, since the Jacobian matrix that occurs in solving the algebraic system of nodal equations arising in such an analysis would tend toward singularity as $\tilde{Ra}\rightarrow\tilde{Ra}^c$. Consequently, the two types of analyses appear to complement each other.

One of the goals of this analysis was to track solution branches as a function of the Rayleigh number. The weakly non-linear technique that was used herein is particularly convenient for this task since it only requires the solution of a small system of non-linear algebraic equations for each new value of $\tilde{Ra}$. Furthermore, this task was efficiently automated by the use of a first-order continuation scheme. Nonetheless, an initial solution must still be obtained on each solution branch that is to be tracked, and in some cases this proved to be a difficult, and tedious, undertaking. (Note that this is also a problem for local schemes.) This was particularly true for the solutions that were sought for binary fluid mixtures, probably as a result of the increased complexity of the governing equations. It is suggested that a homotopy continuation technique be used, which should, in theory, allow the determination of all of the solutions to the algebraic equations resulting from a particular truncation within a prescribed subspace of the function space spanned by the functions in the representation.

The results for monocomponent systems indicate that non-linear effects are important for cylinder aspect ratios near one or greater. In general, non-linear behaviour was observed to become important for fluids with low Prandtl numbers at reduced Rayleigh numbers compared to fluids with higher Prandtl numbers. Nevertheless, the qualitative behaviour of systems with different Prandtl numbers was typically very similar in many respects. The primary exception to this was the tendency of low Prandtl number solutions to become unstable to oscillatory instabilities for $\gamma>1$, which was not observed for higher Prandtl number fluids over the accessible Rayleigh-number range. This finding agrees qualitatively with the experimental observations of Müller *et al.*[7]

The weakly non-linear theory successfully predicted secondary branches whose existence is supported by experimental observations. However, the quantitative accuracy of the solutions along these branches is not known, since it seems possible that a higher degree of non-linearity may be required to describe accurately the physics than was accounted for in this analysis. The linear stability theory suggests a complex correspondence between the spatial structure of the flow solutions and the cylinder aspect ratio. This correspondence was verified by the non-linear theory, although the non-linear results suggest that the 'patches' of aspect ratio over which higher modes ($n \geqslant 2$) are the critical mode are primarily indicative of the likelihood of bifurcations to stable secondary branches at low Rayleigh numbers, rather than of a particular spatial structure of the finite-amplitude solutions.

For binary fluid mixtures, it was found that a relatively small amount of Soret diffusion, as determined by a small value of S, could substantially change the branch structure near the onset of convection. This is particularly true if κ/D is large, reflecting a large separation between the conduction and diffusion time scales, resulting in a large value of ψ. The tendency toward fewer, larger aspect-ratio rolls (length-to-depth) when the Soret effect is active, which was discovered from linear stability theory, was found to persist at higher Rayleigh numbers. In agreement with experimental observations, incipient flow in binary systems, which occurs at a reduced Rayleigh number as a result of the Soret effect (when $\psi > 0$), was found to be weak. Nonetheless, the resulting 3D disturbances to the concentration field were found to be significant. Furthermore, it was determined that these results could be explained in terms of the different mechanism leading to the early onset of convection in binary systems as compared to monocomponent systems. For binary systems heated from below, the destabilization provided by the Soret effect depends on the *timescale* for diffusion. When this timescale is long, perturbations in concentration dissipate slowly, which destabilizes the mixture.

ACKNOWLEDGEMENTS

The authors would like to thank Daniel Henry for many very helpful discussions regarding general formulations of the equations and the consequent roles of the numerous parameters. These discussions have also aided our physical insight. We wish to acknowledge the Scientific Affairs Division of NATO for providing support for this research. In addition, we would like to acknowledge support provided by NASA through the Center for Low-gravity Fluid Mechanics and Transport Phenomena at the University of Colorado. We would also like to acknowledge the John von Neumann National Computer Center for providing computer resources. Finally, R.L.S. would like to acknowledge the support of the National Science Foundation through Grant CTS-8821687.

APPENDIX I: NOMENCLATURE

$\mathbf{A}$	solution vector for equations (19) and (20)
A_{jknl}	coefficients in the velocity-field representation
B_{jknl}	coefficients in the temperature-field representation
C_{jknl}	coefficients in the η-field representation
D	mass diffusivity
D_{jknl}	coefficients in nonaxisymmetric velocity-field representation
D'	Soret coefficient
D''	Dufour coefficient
$\mathbf{e}_r, \mathbf{e}_\theta, \mathbf{e}_z$	cylindrical unit vectors
$\mathbf{F}$	right-hand-side matrix for equations (19) and (20)
L	height of cylinder

$\mathbf{M}$	right-hand-side matrix of equations (19) and (20)
n	azimuthal wave number (mode number)
$\mathbf{n}$	unit normal vector
$\mathbf{O}_{jknl}$	axisymmetric velocity basis function
p	pressure
$\tilde{Pr}$	modified Prandtl number (for a binary fluid)
R	radius of cylinder
Ra	Rayleigh number (for a monocomponent fluid)
$\tilde{Ra}$	modified Rayleigh number (for a binary fluid)
$\tilde{Ra}_{nl}$	modal Rayleigh number from the linear stability problem
r	radial co-ordinate
S	Soret separation number
$\tilde{Sc}$	Schmidt number
T	temperature
T_{B}	temperature of cylinder bottom
T_{T}	temperature of cylinder top
ΔT	$\equiv T_{\mathrm{B}} - T_{\mathrm{T}}$
$\bar{T}$	horizontally averaged temperature
t	time
$\mathbf{u}$	velocity
$\mathbf{U}$	spatial dependence of $\mathbf{u}$ in the linear stability problem
V	volume of cylinder
$\mathbf{V}_{jknl}$	non-axisymmetric velocity basis function
W_1	mass fraction of substance 1
$\tilde{W}_i$	volume-averaged weight fraction of substance i
$\mathbf{W}_{jknl}$	non-axisymmetric velocity basis function
X_{Xe}	mole fraction of xenon
z	vertical co-ordinate

Greek symbols

γ	cylinder aspect ratio ($\equiv R/L$)
ζ	dimensionless Dufour parameter
η	transformed concentration variable
$\bar{\eta}$	horizontally averaged η
Θ	spatial dependence of T in linear stability problem
θ	azimuthal co-ordinate
Λ_{jknl}	η basis function
ξ_{jlt}	complex amplification factor for the linearized horizontally averaged problem
σ	complex amplification factor for the original linear stability problem
Φ_{jknl}	temperature basis function
χ	complex amplification factor for disturbances to non-linear steady states
ψ	dimensionless Soret parameter

Superscripts

c	critical Rayleigh number
D	dimensional quantity
R	rescaled variable
S	steady-state solution

Subscripts

1	property of component one
2	property of component two
B	evaluated at the bottom of the cylinder
n	corresponds to mode n
T	evaluated at the top of the cylinder

APPENDIX II: COMMENTS AND CORRECTIONS FOR PART I

There are some noteworthy corrections besides a few typos and some additional comments extending and clarifying some aspects of Part I.

The Ra appearing in the ordinate of Figures 2–8 should be replaced by $\mathscr{R}=\gamma^4 Ra$. The Ra that appear as the ordinate in Figures 9–12 and 15–22 should be replaced by Ra. In all cases (i.e. replacing Ra by $\mathscr{R}$ or Ra by Ra), all of the subscripts, superscripts or other additional notation should be retained, except that the tilde should be removed from the ordinate of Figures 2 and 3, yielding simply $\mathscr{R}^c$.

It can be shown by manipulating equations (33) and (34) that Figures 15–22 are also valid when the Dufour effect is included if $\tilde{Ra}_n$ is replaced by $Ra_n(1+S)/F_D$. In a similar manner, the asymptotic limit $\psi\to\infty$ discussed on p. 109 can be generalized to include the Dufour effect. The more general statement is $Ra_n(1+S)/F_D\to f(\gamma)/\psi$ as $\psi\to\infty$.

If the results in Table III are recast in terms of $Ra^c(1+S)$ or Ra^c instead of $\tilde{Ra}^c$ (i.e. in terms of a Rayleigh number that does not contain the Dufour parameter in its definition), the anomolous stabilization of the Dufour effect in some cases discussed on p. 100 can be shown to be an artifact of using $\tilde{Ra}^c$. In all cases the Dufour effect is destabilizing.

Finally, the discussion of the limiting case $S\to -1$ (p. 85) is misleading and somewhat erroneous. If one focuses on $Ra(1+S)\psi/F_D$ instead of $\tilde{Ra}$ as was done in that discussion, one can correctly reason that the system is unstable. By utilizing this 're-scaling', it shows that in this limit there is a change in the mechanism causing the instability. The previously reported result is one which would be expected if the mechanism were the usual unstable mean density gradient, but in this limiting case the mechanism is due to the disparity in time scales between heat and mass transfer which can lead to an instability even in the case of a stable mean density gradient. (See Reference 22 for additional discussion of these points.)

REFERENCES

1. G. R. Hardin, R. L. Sani, D. Henry and B. Roux, 'Buoyancy-driven instability in a vertical cylinder: binary fluids with Soret effect. Part I: General theory and stationary stability results', *Int. j. numer. methods fluids*, **10,** 79–117 (1990).
2. W. Eckhaus, *Studies in Non-Linear Stability Theory*, Vol. 6, Springer, Berlin, 1965.
3. G. R. Hardin, 'Buoyancy-driven convection in a vertical cylinder: binary fluid mixtures with Soret effect', *Ph.D. Thesis*, University of Colorado, Boulder, CO, 1987.
4. S. Rosenblat, 'Asymptotic methods for bifurcation and stability problems,' *Stud. Appl. Math.*, **60,** 241–259 (1979).
5. S. Rosenblat, 'Thermal convection in a vertical circular cylinder', *J. Fluid Mech.*, **122,** 395–410 (1982).
6. S. Rosenblat, S. H. Davis and G. M. Homsy, 'Nonlinear Marangoni convection in bounded layers. Part 1. Circular cylindrical containers', *J. Fluid Mech.*, **120,** 91–122 (1982).
7. G. Müller, G. Neumann and W. Weber, 'Natural convection in vertical Bridgman configurations', *J. Cryst. Growth*, **70,** 78–93 (1984).
8. G. S. Charlson and R. L. Sani, 'On thermoconvective instability in a bounded cylindrical fluid layer', *Int. J. Heat Mass Transfer*, **14,** 2157–2160 (1971).
9. J. C. Buell and I. Catton, 'The effect of wall conduction on the stability of a fluid in a right circular cylinder heated from below', *J. Heat Transfer*, **105,** 255–260 (1983).
10. C. S. Yih, 'Thermal instability of viscous fluids', *Q. Appl. Math.*, **17,** 25–42 (1959).
11. J. M. Olson and F. Rosenberger, 'Convective instabilities in a closed vertical cylinder heated from below. Part 1. Monocomponent gases', *J. Fluid Mech.*, **92,** 609–629 (1979).

12. P. Bontoux, personal communication, 1986.
13. G. Neumann, Berechnung der thermischen Auftriebskonvektion in Modellsystemen zur Kristallzüchtung, Der Technischen Fakultät der Universität Erlangen-Nürnberg, zur *Erlangung des Grades Doktor–Ingenieur*, 1986.
14. K. Stork and U. Müller, 'Convection in boxes: an experimental investigation in vertical cylinders and annuli', *J. Fluid Mech.*, **71,** 231–240 (1975).
15. G. Iooss and D. D. Joseph, *Elementary Stability and Bifurcation Theory*, Springer, New York, 1980.
16. J. R. Abernathey and F. Rosenberger, 'Soret diffusion and convective stability in a closed vertical cylinder', *Phys. Fluids*, **24,** 377–381 (1981).
17. Y. S. Touloukain (Ed.), *Thermophysical Properties of Matter*, Plenum, New York, 1970.
18. C. B. Garcia and W. I. Zangwill, *Pathways to Solutions, Fixed Points, and Equilibria*, Prentice Hall, Englewood Cliffs, NJ, 1981.
19. D. T. J. Hurle and E. Jakeman, 'Soret-driven thermosolutal convection', *J. Fluid Mech.*, **47,** 667–687 (1971).
20. F. R. Winter and H. G. Drickamer, 'Thermal diffusion in liquid metals', *J. Phys. Chem.*, **59,** 1229–1230 (1955).
21. S. R. Corriell, M. R. Cordes, W. J. Boettinger and R. F. Sekerka, 'Convective and interfacial instabilities during unidirectional solidification of a binary alloy', *J. Cryst. Growth*, **49,** 13–28 (1980).
22. D. Henry, G. Hardin, B. Roux and R. Sani, 'Instability with Soret effect: the globalized formulation, its physical interpretation and specific solution for long cylinders', *Int. Symp. Hydrodynamics and Heat/Mass-Transfer in Microgravity*, 6–12 July 1991, Perm-Yaroslavl, Russia.